

## Stimulated Raman Amplification in GaAs/AlAs Intermixed Superlattices


Isao Tomita,<sup>1,2,\*</sup> Shinichi Saito,<sup>1,3</sup> and David C. Hutchings<sup>4</sup>

<sup>1</sup>*Sustainable Electronic Technologies, School of Electronics and Computer Science, University of Southampton, Southampton SO17 1BJ, United Kingdom*

<sup>2</sup>*Department of Electrical and Computer Engineering, National Institute of Technology, Gifu College, Motosu 501-0495, Japan*

<sup>3</sup>*Zepler Institute, Faculty of Physical Sciences and Engineering, University of Southampton, Southampton SO17 1BJ, United Kingdom*

<sup>4</sup>*School of Engineering, University of Glasgow, Glasgow G12 8QQ, United Kingdom*

 (Received 17 October 2017; revised manuscript received 27 May 2018; published 4 December 2018)

The enhancement of stimulated Raman scattering (SRS) with a GaAs/AlAs intermixed superlattice that works as a  $\chi^{(3)}$ -quasi-phase-matched structure is studied, where such Kerr-induced effects as four-wave mixing (FWM), self-phase-modulation (SPM), cross-phase-modulation (XPM), and two-photon absorption (TPA) are included. In particular, the efficiency of anti-Stokes generation is enhanced here; anti-Stokes generation inherently has an extremely small efficiency due to a phase mismatch in the interaction of the pump, Stokes, and anti-Stokes waves (while the efficiency of Stokes generation is sufficiently large because of no such phase mismatch). The superlattice enhances the anti-Stokes efficiency up to the order of  $10^3$  when compared with that without the superlattice, particularly at a small pump intensity. In this enhancement, it is seen that there is an efficiency boost via simultaneous FWM. In this situation, it is shown how much SPM and XPM degrade the efficiency enhancement. Furthermore, an optimal superlattice length is identified that provides the highest efficiency. The degradation of the efficiency at the optimized length due to TPA is also analyzed. Finally, to gain more anti-Stokes efficiency (or control the sizes of the Stokes and anti-Stokes efficiencies), a photonic-band-gap cavity structure is proposed.

DOI: [10.1103/PhysRevApplied.10.064005](https://doi.org/10.1103/PhysRevApplied.10.064005)

### I. INTRODUCTION

Studies on the enhancement of stimulated Raman scattering (SRS) have been attracting a great deal of attention in recent years, aiming for its potential scientific and technological applications; for example, probing, sensing [1,2], optical on-chip [3–7], and telecom [8,9] applications. Among them, the realization of SRS in silicon (Si) [3–7] gave a great impetus to the development of Si on-chip optical devices at telecom wavelengths, which provided a potential integrated optical source with Si photonics. However, there still remains an issue that large two-photon absorption (TPA) in Si at around  $1.55 \mu\text{m}$  must be avoided for practical applications and yet cannot easily be resolved because the band-gap energy (1.1 eV) of Si is much smaller than the TPA energy ( $2 \times 0.8 = 1.6 \text{ eV}$ ) of  $1.55\text{-}\mu\text{m}$  optical signals.

Semiconductor optical amplifiers [10] made of compound semiconductors can avoid TPA via band-gap engineering with composition-ratio and/or strain controls, but their carriers, or electron-hole pairs, which give rise to radiative recombination for optical signal amplification, distort the signal waveforms via plasma effects, thus preventing the operation speed from going beyond tens of gigahertz without additional systems.

Fortunately, silica-glass optical fibers ( $\text{SiO}_2$ , insulator with no carriers) have a wide band gap that can avert TPA at around  $1.55 \mu\text{m}$ , but their Raman gain coefficient  $g$  (cm/GW) is very small compared with that of semiconductors [e.g., Si, GaP,  $\text{Al}_x\text{Ga}_{1-x}\text{As}$ ] (see Table I), thus requiring a very long fiber on the order of kilometers.

Here we propose a compact device design that uses compound-semiconductor superlattices that can avoid TPA while using the third-order optical nonlinearity enhancement, and examine the enhancement behaviors from nonlinear optical physics, where the use of instantaneous nonlinear interactions (with no TPA) provides this superlattice device with potential that goes beyond the current operation limitations of Si photonic devices and semiconductor optical amplifiers.

\*I.Tomita@soton.ac.uk

Published by the American Physical Society under the terms of the [Creative Commons Attribution 4.0 International](https://creativecommons.org/licenses/by/4.0/) license. Further distribution of this work must maintain attribution to the author(s) and the published article's title, journal citation, and DOI.

TABLE I. Properties of Raman materials.

Material type	Raman gain (cm/GW)	Raman shift (nm)	Pump wavelength (nm)	Device length (mm)	References
SiO <sub>2</sub>	0.0065	105.6	1433	$5.6 \times 10^6$	[8]
Si	20	124.8	1427	18	[4]
GaP	27	27.6	825	5.1	[11]
H <sub>2</sub>	4.4	117.6	532	$\sim 10^3$	[12,13]
Ba(NO <sub>3</sub> ) <sub>2</sub>	47.4	29.6	532	$\sim 10^2$	[14,15]
Al <sub>0.24</sub> Ga <sub>0.76</sub> As	10	70.8	1550	7.2	[16]

### A. Research target, method, and applications

In this paper, we focus on a merit of our device that can boost the output efficiency of the anti-Stokes waves that originally have a vanishingly small efficiency due to a large phase mismatch  $\Delta\mathbf{k} = 2\mathbf{k}_0 - \mathbf{k}_{-1} - \mathbf{k}_1$  that arises in the interacting pump, Stokes, and anti-Stokes waves of wavevectors  $\mathbf{k}_0$ ,  $\mathbf{k}_{-1}$ , and  $\mathbf{k}_1$ , respectively [17]. Fortunately, the Stokes waves are strongly generated in this device because of the absence of such a phase-mismatch requirement. The ratio of the anti-Stokes-wave power to the Stokes-wave power, for example, in Si waveguides, is only  $10^{-6}$ – $10^{-5}$  [18,19]. However, our proposed device should provide the same order of output power for both Stokes and anti-Stokes waves, as seen in Sec. IV B 4. An application of the anti-Stokes-wave amplification with our device is that since it generates a short wavelength (e.g.,  $1.49 \mu\text{m}$ ) from an input pump beam (e.g., at  $1.56 \mu\text{m}$ ), it can amplify the downstream signals at  $1.49 \mu\text{m}$  in gigabit-Ethernet passive optical networks [20]. It can also be used for channel conversion and amplification in wavelength-division multiplexing systems.

To attain high amplification by removal of  $\Delta\mathbf{k}$ , we use quasi-phase-matching [21] for  $\chi^{(3)}$  processes in a collinear beam configuration (e.g., in a waveguide) that gives a strong field coupling among those three waves and thus achieves high output efficiency. In this paper, instead of quasi-phase-matched (QPM) structures proposed in SiO<sub>2</sub>, Ba(NO<sub>3</sub>)<sub>2</sub>, and H<sub>2</sub> [12,14], which are not easily fabricated, we use a GaAs/AlAs intermixed superlattice, which was originally developed as a  $\chi^{(2)}$ -periodic QPM structure [22]. This has a small refractive-index change (approximately 0.01) in  $\chi^{(2)}$  domains (i.e., only a 0.3% change compared with the average refractive index in the periodic structure) [23], and has an advantage of avoiding significant additional optical scattering loss caused by interface roughness between the discrete  $\chi^{(2)}$  domains; for example, in orientation-patterned Al<sub>x</sub>Ga<sub>1-x</sub>As structures [24].

An important aspect in the GaAs/AlAs intermixed superlattice is that it also works as a  $\chi^{(3)}$ -periodic QPM structure because a  $\chi^{(3)}$  change is also induced in a similar way to the  $\chi^{(2)}$  change caused by blueshifted resonance in nonlinear susceptibility [25]. The removal of  $\Delta\mathbf{k}$  with this  $\chi^{(3)}$ -periodic structure realizes strong anti-Stokes-wave

generation. Although the aforementioned  $\chi^{(3)}$ -periodic superlattice still has  $\chi^{(2)}$  periodicity, the anti-Stokes waves are not influenced, for example, by difference-frequency generation (DFG) with  $\chi^{(2)}$ , when the  $\chi^{(3)}$  period  $\Lambda$  is set such that  $|2\mathbf{k}_0 - \mathbf{k}_{-1} - \mathbf{k}_1| = 2\pi/\Lambda$ , because DFG requires  $|\mathbf{k}_0 - \mathbf{k}_{-1} - \mathbf{k}_1| = 2\pi/\Lambda$  [26].

Although the above discussion does not include a backward scattering of the beams caused by the periodic refractive-index structure, its omission is justified by the calculations given in the Appendix, and the phase matching using Bloch harmonics that arise from the same periodic structure is not used here because of no usefulness due to the very small refractive-index difference (0.3%) in the periodic structure.

### B. Device physics research

In our semiconductor  $\chi^{(3)}$ -periodic structure, we carefully examine the anti-Stokes-wave generation in terms of the pump intensity and the device length because of our interest in highly efficient output with a moderate pump intensity and a reasonable device length.

Furthermore, we carefully examine other nonlinear effects (Kerr-induced effects), such as four-wave mixing (FWM), self-phase-modulation (SPM), and cross-phase-modulation (XPM), because these are much greater than those in Si. With regard to TPA, since the band-gap energy in the GaAs/AlAs superlattice is comparable to the TPA energy (1.6 eV), TPA can be avoided by subtle input-wavelength adjustment or band-gap engineering, which can be done easily when compared with the Si case.

The influence of stimulated Brillouin scattering (SBS) coupled with low-frequency acoustic-phonon modes is ignored here because, for example, in GaAs [27], the Brillouin-shifted frequency and its linewidth are only  $f_{\text{SBS}} \sim 20 \text{ GHz}$  and  $\Delta f_{\text{SBS}} \sim 170 \text{ MHz}$ , respectively. Thus, if we use relatively short input pulses (e.g., with a width of approximately 10 ps or a spectral width of approximately 100 GHz as used often in optical communications), SBS nearly ceases to occur because most of the spectral components are out of the SBS gain linewidth  $\Delta f_{\text{SBS}}$ . This SBS-stopping phenomenon is well known in optical fibers for short pump pulses [28]. On the other hand, since SRS coupled with high-frequency optical-phonon modes

has a much wider gain linewidth  $\Delta f_{\text{SRS}} \sim 100$  GHz, SRS can keep its large gain (e.g., for the 10-ps pulses) at the Raman-shifted frequency  $f_{\text{SRS}} \sim 9$  THz [16].

In this way, while including such nonlinear interactions as optical Raman and Kerr effects in the proposed periodic structure, we examine the SRS efficiency; more specifically, we examine the SRS efficiency of anti-Stokes waves, with a far smaller efficiency than Stokes waves.

### C. Paper structure

After this introduction, we describe a model for the periodic GaAs/AlAs intermixed superlattice in Sec. II. We then derive coupled nonlinear equations that deal with the interacting pump, Stokes, and anti-Stokes waves in the superlattice in Sec. III. In Sec. IV, we obtain analytical solutions with some approximations to the coupled equations to see the properties of those nonlinear effects on the output efficiency. Furthermore, we obtain numerical solutions that contain no such approximations, and compare them with the analytical solutions to check numerical accuracy. The numerical computations give the efficiency when there is a superlattice, which is compared with the efficiency without the superlattice, and improvements are discussed. Finally, Sec. V is devoted to a summary.

## II. MODEL FOR A $\chi^{(3)}$ -PERIODIC SUPERLATTICE

We show our device model, which contains a periodic GaAs/AlAs intermixed superlattice, in Fig. 1, where the pump, Stokes, and anti-Stokes wavelengths are greater than the half-band-gap wavelength of the superlattice, which prevents TPA. (The influence of TPA is examined in detail in Sec. IV B 7.)

In the case where one of those three wavelengths is shorter than the half-band-gap wavelength, strong TPA

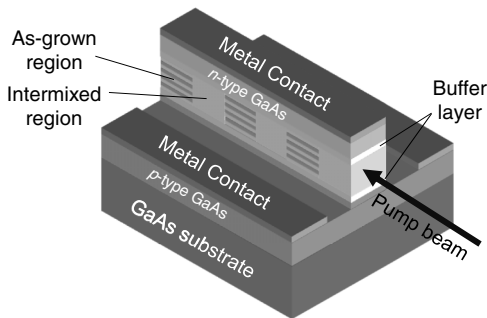


FIG. 1. Device structure. A GaAs/AlAs superlattice containing periodic as-grown and intermixed regions is sandwiched between buffer layers that have a lower refractive index than the waveguide to confine light in it, where the thickness of the buffer layers is adjusted to strongly confine the light, and the waveguide together with the buffer layers is also sandwiched between  $p$ -type GaAs and  $n$ -type GaAs to form a  $p$ - $n$  junction.

will emerge, and considerable free-carrier absorption (FCA) will also emerge due to TPA-induced carriers. In this case, we use a reverse-biased  $p$ - $n$  junction embedded in the device to avert FCA, as shown in Fig. 1, where the superlattice waveguide is sandwiched between buffer layers of  $\text{Al}_x\text{Ga}_{1-x}\text{As}$  with  $x = 0.56$  or  $0.6$  [23] with a lower refractive index than the waveguide. If those three wavelengths are longer than the half-band-gap wavelength, such a  $p$ - $n$  junction is not necessary (or no bias-voltage application is necessary for the  $p$ - $n$  junction).

When the as-grown domains of the waveguide in Fig. 1 are made of a 14:14 monolayer GaAs/AlAs superlattice, the  $\chi^{(3)}$  characteristic can be well approximated by that of  $\text{Al}_x\text{Ga}_{1-x}\text{As}$  ( $x = 0.18$ ) [29], which has a fundamental absorption edge almost identical to that of the 14:14 monolayer GaAs/AlAs superlattice. In our calculations for the GaAs/AlAs as-grown domains, we use this  $\text{Al}_x\text{Ga}_{1-x}\text{As}$  ( $x = 0.18$ ), which makes the calculations simpler.

On the other hand, the intermixed regions have a blueshifted absorption edge as regards the  $\chi^{(3)}$  property, and the  $\chi^{(3)}$  value is considerably decreased when compared with that in the as-grown domains (it is nearly a half of  $\chi^{(3)}$ ) [29]. We set this value to be  $\varepsilon\chi^{(3)}$  ( $0 \leq \varepsilon \leq 1$ ) in our calculations, as shown in Sec. IV B 4. In the next section, we derive coupled nonlinear equations to describe the evolution of the pump, Stokes, and anti-Stokes waves for the waveguide device.

## III. COUPLED NONLINEAR EQUATIONS FOR THE DEVICE

In deriving the coupled nonlinear equations, we assume that SRS is greater in photon generation than in spontaneous Raman scattering (i.e., beyond the SRS threshold power) [17]. In this case, since there is almost no difference in optical power obtained by classical and quantum analyses, we describe SRS in the waveguide device with classical wave equations derived from Maxwell's equations that are coupled with molecular vibrations in the semiconductor used.

To perform the analysis for SRS, we start with the following wave equations obtained via the standard procedure [30]:

$$\nabla^2 E - \frac{1}{c^2} \frac{\partial^2 E}{\partial t^2} = \mu_0 \frac{\partial^2}{\partial t^2} (P_{\text{LN}} + P_{\text{NL}}), \quad (1)$$

$$\nabla^2 E - \frac{1}{c^2} \frac{\partial^2 (\varepsilon E)}{\partial t^2} = \mu_0 \frac{\partial^2 P_{\text{NL}}}{\partial t^2}, \quad (2)$$

where  $\nabla^2 = \partial^2/\partial x^2 + \partial^2/\partial y^2 + \partial^2/\partial z^2$ . The waveguide is set parallel to the  $z$  direction.  $E = E(z, t)$  is the electric field of the three coupled waves (i.e., the pump, Stokes, and anti-Stokes waves) that propagate in the  $z$  direction.  $P_{\text{LN}}$  is the linear polarization defined by  $P_{\text{LN}} = \varepsilon_0 \chi^{(1)} E$  with

vacuum permittivity  $\epsilon_0$  and linear susceptibility  $\chi^{(1)}$ . The relative permittivity  $\epsilon$  is related to  $\chi^{(1)}$  as  $\epsilon = 1 + \chi^{(1)}$ , which gives the refractive index  $n$  as  $n = \sqrt{\epsilon}$ .  $P_{\text{NL}}$  is the nonlinear polarization containing the Raman and Kerr effects, and  $\mu_0$  is the magnetic permeability. Nonmagnetic semiconductors (e.g.,  $\text{Al}_x\text{Ga}_{1-x}\text{As}$ ) have the same value as  $\mu_0$  in a vacuum. The velocity of light  $c$  is related to  $\epsilon_0$  and  $\mu_0$  by  $c = 1/\sqrt{\epsilon_0\mu_0}$ . In the above, TE polarization is assumed for  $E$ ,  $P_{\text{LN}}$ , and  $P_{\text{NL}}$ , which are excited by TE-mode pump lasers.

The nonlinear polarization for the Raman effect is given by [14,31]

$$P_{\text{NL}}^R = \epsilon_0 \chi^{(3)} Q E, \quad (3)$$

$$\frac{\partial^2 Q}{\partial t^2} + \frac{2}{\tau} \frac{\partial Q}{\partial t} + \omega_v^2 Q = \gamma E^2, \quad (4)$$

where  $\chi^{(3)}$  is the imaginary part of the third-order nonlinear susceptibility,  $Q$  is the phonon-wave amplitude,  $\omega_v$  is the Raman frequency,  $\tau$  is the relaxation time of the molecular oscillation, and  $\gamma$  is a constant that characterizes the coupling between electric fields and polarized molecules. In addition, the nonlinear polarization for the Kerr effect is given by [28]

$$P_{\text{NL}}^K = \epsilon_0 \chi^{(3)} E^3, \quad (5)$$

where  $\chi^{(3)}$  is the real part of the third-order nonlinear susceptibility. Experimentally, the Kerr effect arises together with the Raman effect [32], and thus the total nonlinear polarization  $P_{\text{NL}}$  is expressed as the sum of Eqs. (3) and (5).

In the above, the tensor component in the third-order nonlinear susceptibility is chosen such that TE-mode input gives TE-mode output.

### A. Simplification of the space and time derivatives of the wave equation

The space and time derivatives on the left-hand side of the wave equation [Eq. (2)] are simplified when we use an optical pulse with spatial width greater than the characteristic length of the waves (i.e., the wavelength). This is known as the ‘‘slowly-varying-envelope approximation’’ [30]. We use this approximation throughout the paper.

To express  $\epsilon E$  in Eq. (2) containing the three waves, we use the following sum of electric fields:

$$\epsilon E = \frac{1}{2} \left[ \sum_j \epsilon_j E_j e^{i(k_j z - \omega_j t)} + \text{c.c.} \right], \quad (6)$$

where  $j = -1, 0, 1$  stand for the Stokes, pump, and anti-Stokes waves, respectively,  $\omega_j$  is the frequency of the  $j$ th wave, and  $\epsilon_j$  is the  $\omega_j$  component of  $\epsilon$  [i.e.,  $\epsilon_j = \epsilon(\omega_j)$ ], and  $k_j$  is the wavenumber of the  $j$ th wave. Using the

Raman frequency  $\omega_v$ , we can write  $\omega_j$  as  $\omega_j = \omega_0 + j\omega_v$ . The Stokes and anti-Stokes waves ( $j = -1, 1$ ) that we deal with here are the first excited ones. Since the growth of excited waves of order higher than the first excited waves needs a much longer interaction length than that for the first excited waves [14], and since we are interested in a relatively short waveguide on the order of 1 cm, the emergence of higher-order excited waves is ignored.

If we set  $\epsilon = \epsilon_j = 1$  in Eq. (6), the expansion of  $E$  takes the form

$$E = \frac{1}{2} \left[ \sum_j E_j e^{i(k_j z - \omega_j t)} + \text{c.c.} \right]. \quad (7)$$

In Eq. (2), we insert Eq. (6) into  $\partial^2(\epsilon E)/\partial t^2$  and Eq. (7) into  $\nabla^2 E$ , where the relation  $\partial^2 E/\partial x^2 = \partial^2 E/\partial y^2 = 0$  holds because of the assumption  $E = E(z, t)$ . The spread of the electric fields in the  $x$  and  $y$  directions is included as a constant cross-section area of the waveguide.

A simplified equation for the left-hand side of Eq. (2) by substitution of Eq. (7) for  $\partial^2 E/\partial z^2$  is of the form

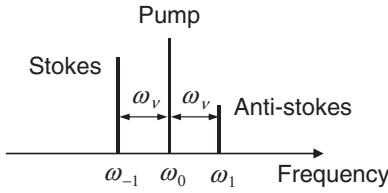
$$\begin{aligned} \frac{\partial^2 E}{\partial z^2} &= \frac{1}{2} \left[ \sum_j \frac{\partial^2 E_j}{\partial z^2} e^{i(k_j z - \omega_j t)} + 2 \sum_j i k_j \frac{\partial E_j}{\partial z} e^{i(k_j z - \omega_j t)} \right. \\ &\quad \left. - \sum_j k_j^2 E_j e^{i(k_j z - \omega_j t)} + \text{c.c.} \right] \\ &\approx \sum_j i k_j \frac{\partial E_j}{\partial z} e^{i(k_j z - \omega_j t)} - \sum_j \frac{k_j^2}{2} E_j e^{i(k_j z - \omega_j t)} + \text{c.c.} \end{aligned} \quad (8)$$

Also, by substituting Eq. (6) for  $\partial^2(\epsilon E)/\partial t^2$ , we obtain

$$\begin{aligned} \frac{\partial^2(\epsilon E)}{\partial t^2} &\approx - \sum_j i \epsilon_j \omega_j \frac{\partial E_j}{\partial t} e^{i(k_j z - \omega_j t)} \\ &\quad - \sum_j \epsilon_j \frac{\omega_j^2}{2} E_j e^{i(k_j z - \omega_j t)} + \text{c.c.} \end{aligned} \quad (9)$$

Inserting Eqs. (8) and (9) into the left-hand side of Eq. (2) with the relation  $\epsilon_j = n_j^2$  ( $n_j$  is the refractive index for the  $j$ th wave), we obtain

$$\begin{aligned} \nabla^2 E - \frac{1}{c^2} \frac{\partial^2(\epsilon E)}{\partial t^2} &\approx \sum_j e^{i(k_j z - \omega_j t)} \left( i k_j \frac{\partial}{\partial z} + i \frac{n_j^2}{c^2} \omega_j \frac{\partial}{\partial t} \right) E_j + \text{c.c.} \\ &= \sum_j e^{i(k_j z - \omega_j t)} i k_j \left( \frac{\partial}{\partial z} + \frac{n_j}{c} \frac{\partial}{\partial t} \right) E_j + \text{c.c.}, \end{aligned} \quad (10)$$


 FIG. 2. Relation of  $\omega_{-1}$ ,  $\omega_0$ ,  $\omega_1$ , and  $\omega_v$ .

where the relation  $\omega_j = (c/n_j)k_j$  is used. By replacing  $n_j$  ( $j = -1, 0, 1$ ) with the averaged value  $n = \langle n_j \rangle$  in Eq. (10), we can further simplify the space and time derivatives of Eq. (10). This replacement does not severely affect the results because the refractive-index deviation ( $\Delta n \approx 0.01$ ) from  $n$  is only 0.3% of  $n = \langle n_j \rangle = 3.09$ , which is obtained from  $n_j \approx 3.08\text{--}3.10$  at 1450–1600 nm [23]. We then use the transformations  $z_{\text{new}} = z_{\text{old}}$  and  $t_{\text{new}} = t_{\text{old}} - (n/c)z_{\text{old}}$  [28], and obtain

$$ik_j \left( \frac{\partial}{\partial z} + \frac{n}{c} \frac{\partial}{\partial t} \right) E_j = ik_j \frac{\partial}{\partial z} E_j. \quad (11)$$

This transformation corresponds to a frame change such that the optical pulse in the waveguide is observed from a moving coordinate in the  $z$  direction with a velocity of  $c/n$ .

### B. Derivation of terms for the Raman effect

To derive the coupled equations of the three waves with  $j = -1, 0, 1$ , we first need to extract nonlinear polarization terms for the Raman effect that satisfy  $\omega_0 - \omega_{-1} = \omega_v$  and  $\omega_1 - \omega_0 = \omega_v$ , which we call ‘‘resonant terms.’’ Here  $\omega_{-1}$ ,  $\omega_0$ , and  $\omega_1$  stand for the frequencies of the Stokes, pump, and anti-Stokes waves, respectively. The relation of  $\omega_{-1}$ ,  $\omega_0$ ,  $\omega_1$ , and  $\omega_v$  is illustrated in Fig. 2.

To calculate the nonlinear polarization in Eq. (3), we insert the electric field  $E$  in Eq. (7) and the following phonon-wave amplitude  $Q$  into Eq. (3):

$$Q = \frac{1}{2} [q e^{i(k_v z - \omega_v t)} + \text{c.c.}], \quad (12)$$

where  $k_v$  is the wavenumber of the phonon wave with a frequency of  $\omega_v$ . By this insertion, we have

$$P_{\text{NL}}^R = \frac{\epsilon_0 \chi^{(3)}}{4} \left\{ \sum_j q E_{j-1} e^{i[(k_{j-1} + k_v)z - \omega_j t]} + q^* E_{j+1} e^{i[(k_{j+1} - k_v)z - \omega_j t]} + \text{c.c.} \right\}. \quad (13)$$

Next we obtain the second-order time derivative of  $P_{\text{NL}}^R$ , which is necessary for the calculation of the right-hand side

of Eq. (2):

$$\mu_0 \frac{\partial^2 P_{\text{NL}}^R}{\partial t^2} \approx -\frac{\epsilon_0 \mu_0 \chi^{(3)}}{4} \left\{ \sum_j \omega_j^2 q E_{j-1} e^{i[(k_{j-1} + k_v)z - \omega_j t]} + \omega_j^2 q^* E_{j+1} e^{i[(k_{j+1} - k_v)z - \omega_j t]} + \text{c.c.} \right\}, \quad (14)$$

where the slowly-varying-envelope approximations,  $|\omega_j q| \gg |\partial q / \partial t|$ ,  $|\omega_j E_j| \gg |\partial E_j / \partial t|$ , are used.

To extract resonant terms from Eq. (14) for  $\omega_j$  ( $j = -1, 0, 1$ ), we write down the terms resonant to  $\omega_j$  in Eq. (13) as  $P_R^{(\omega_j)}$  and obtain  $\mu_0 \partial^2 P_R^{(\omega_j)} / \partial t^2$  for  $j = -1, 0, 1$  as

$$\mu_0 \frac{\partial^2 P_R^{(\omega_{-1})}}{\partial t^2} = -\frac{\epsilon_0 \mu_0 \chi^{(3)}}{4} \omega_{-1}^2 q^* E_0 e^{i[(k_0 - k_v)z - \omega_{-1} t]}, \quad (15)$$

$$\mu_0 \frac{\partial^2 P_R^{(\omega_0)}}{\partial t^2} = -\frac{\epsilon_0 \mu_0 \chi^{(3)}}{4} \omega_0^2 \{ q E_{-1} e^{i[(k_{-1} + k_v)z - \omega_0 t]} + q^* E_1 e^{i[(k_1 - k_v)z - \omega_0 t]} \}, \quad (16)$$

$$\mu_0 \frac{\partial^2 P_R^{(\omega_1)}}{\partial t^2} = -\frac{\epsilon_0 \mu_0 \chi^{(3)}}{4} \omega_1^2 q E_0 e^{i[(k_0 + k_v)z - \omega_1 t]}. \quad (17)$$

The  $q$  and  $q^*$  in Eqs. (15)–(17) are related to  $E_j$  via Eqs. (4) and (12). To clarify the relation between them, we calculate Eq. (4) by inserting Eq. (12) into it. This calculation needs the first- and the second-order time derivatives of  $Q$ , which are of the form

$$\frac{\partial Q}{\partial t} = \frac{1}{2} \left[ \frac{\partial q}{\partial t} e^{i(k_v z - \omega_v t)} - i\omega_v q e^{i(k_v z - \omega_v t)} + \text{c.c.} \right], \quad (18)$$

$$\begin{aligned} \frac{\partial^2 Q}{\partial t^2} &= \frac{1}{2} \left[ \frac{\partial^2 q}{\partial t^2} e^{i(k_v z - \omega_v t)} - 2i\omega_v \frac{\partial q}{\partial t} e^{i(k_v z - \omega_v t)} \right. \\ &\quad \left. - \omega_v^2 q e^{i(k_v z - \omega_v t)} + \text{c.c.} \right] \\ &\approx \frac{1}{2} \left[ -2i\omega_v \frac{\partial q}{\partial t} e^{i(k_v z - \omega_v t)} - \omega_v^2 q e^{i(k_v z - \omega_v t)} + \text{c.c.} \right] \\ &= - \left( i\omega_v \frac{\partial q}{\partial t} + \frac{\omega_v^2}{2} q \right) e^{i(k_v z - \omega_v t)} + \text{c.c.}, \end{aligned} \quad (19)$$

where the slowly-varying-envelope approximation is used again.



To obtain the relation between  $q$  (or  $q^*$ ) and  $E_j$ , we substitute Eqs. (18) and (19) into Eq. (4) and obtain

$$\left[ \left( -i\omega_v + \frac{1}{\tau} \right) \frac{\partial q}{\partial t} - i \frac{\omega_v}{\tau} q \right] e^{i(k_v z - \omega_v t)} + \text{c.c.} = \gamma E^2, \quad (20)$$

$$-i\omega_v \left( \frac{\partial q}{\partial t} + \frac{q}{\tau} \right) e^{i(k_v z - \omega_v t)} + \text{c.c.} = \gamma E^2, \quad (21)$$

where the approximation  $\omega_v \gg 1/\tau$  is used, which arises from the relaxation time  $\tau$  that is much greater than the timescale ( $\sim 1/\omega_v$ ) of high molecular eigenfrequencies.

Next we calculate the right-hand side of Eq. (21). Inserting Eq. (7) into it, we obtain

$$\begin{aligned} \gamma E^2 &= \gamma \left\{ \frac{1}{2} \left[ \sum_j E_j e^{i(k_j z - \omega_j t)} + \text{c.c.} \right] \right\}^2 \\ &= \frac{\gamma}{4} \left\{ \sum_j \sum_m E_j E_m e^{i[(k_j + k_m)z - (\omega_j + \omega_m)t]} \right. \\ &\quad \left. + \sum_j \sum_m E_j E_m^* e^{i[(k_j - k_m)z - (\omega_j - \omega_m)t]} + \text{c.c.} \right\}. \quad (22) \end{aligned}$$

Extracting resonant terms from Eq. (22) that satisfy  $\omega_j - \omega_m = \omega_v$  (or  $\omega_j - \omega_{j-1} = \omega_v$ ), and substituting them into

the right-hand side of Eq. (21), we obtain

$$\begin{aligned} &-i\omega_v \left( \frac{\partial q}{\partial t} + \frac{q}{\tau} \right) e^{i(k_v z - \omega_v t)} \\ &= \frac{\gamma}{4} \sum_j E_j E_{j-1}^* e^{i[(k_j - k_{j-1})z - (\omega_j - \omega_{j-1})t]}, \quad (23) \end{aligned}$$

$$\frac{\partial q}{\partial t} = \frac{1}{\tau} \left[ -q - \frac{\gamma\tau}{4i\omega_v} \sum_j E_j E_{j-1}^* e^{i(k_j - k_{j-1} - k_v)z} \right], \quad (24)$$

where  $\omega_j - \omega_{j-1} = \omega_v$  is used.

For  $j = -1, 0, 1$ , Eq. (24) takes the form

$$\begin{aligned} \frac{\partial q}{\partial t} &= \frac{1}{\tau} \left\{ -q - \frac{\gamma\tau}{4i\omega_v} [E_0 E_{-1}^* e^{i(k_0 - k_{-1} - k_v)z} \right. \\ &\quad \left. + E_1 E_0^* e^{i(k_1 - k_0 - k_v)z}] \right\}. \quad (25) \end{aligned}$$

Equation (25) gives the relation that connects  $q$  (or  $q^*$ ) to  $E_j$  ( $j = -1, 0, 1$ ).

### C. Derivation of terms for the Kerr effect

In this section, we calculate the nonlinear polarization [Eq. (5)] for the Kerr effect. To do this, we substitute Eq. (7) into Eq. (5) and obtain

$$\begin{aligned} P_{\text{NL}}^K &= \epsilon_0 \chi^{(3)} \left\{ \frac{1}{2} \left[ \sum_j E_j e^{i(k_j z - \omega_j t)} + \text{c.c.} \right] \right\}^3 \\ &= \frac{\epsilon_0 \chi^{(3)}}{8} \left\{ \sum_j \sum_l \sum_m E_j E_l E_m e^{i[(k_j + k_l + k_m)z - (\omega_j + \omega_l + \omega_m)t]} \right. \\ &\quad \left. + 3 \sum_j \sum_l \sum_m E_j E_l E_m^* e^{i[(k_j + k_l - k_m)z - (\omega_j + \omega_l - \omega_m)t]} + \text{c.c.} \right\}. \quad (26) \end{aligned}$$

By obtaining the second-order time derivative of  $P_{\text{NL}}^K$  necessary to calculate the right-hand side of Eq. (2), we get

$$\begin{aligned} \mu_0 \frac{\partial^2 P_{\text{NL}}^K}{\partial t^2} &\approx -\frac{\epsilon_0 \mu_0 \chi^{(3)}}{8} \left\{ \sum_j \sum_l \sum_m (\omega_j + \omega_l + \omega_m)^2 E_j E_l E_m e^{i[(k_j + k_l + k_m)z - (\omega_j + \omega_l + \omega_m)t]} \right. \\ &\quad \left. + 3 \sum_j \sum_l \sum_m (\omega_j + \omega_l - \omega_m)^2 E_j E_l E_m^* e^{i[(k_j + k_l - k_m)z - (\omega_j + \omega_l - \omega_m)t]} + \text{c.c.} \right\}, \quad (27) \end{aligned}$$

where the slowly-varying-envelope approximation,  $|\omega_j E_j| \gg |\partial E_j / \partial t|$ , is used.

To extract resonant terms from Eq. (27), we write down the terms resonant to  $\omega_j$  in Eq. (26) as  $P_K^{(\omega_j)}$  and obtain

$\mu_0 \partial^2 P_K^{(\omega_j)} / \partial t^2$  for  $j = -1, 0, 1$  as

$$\mu_0 \frac{\partial^2 P_K^{(\omega_{-1})}}{\partial t^2} = -\frac{3\epsilon_0 \mu_0 \chi^{(3)}}{8} \omega_{-1}^2 (|E_{-1}|^2 + 2E_{-1}|E_1|^2 + 2E_{-1}|E_0|^2) e^{i(k_{-1}z - \omega_{-1}t)}, \quad (28)$$

$$\mu_0 \frac{\partial^2 P_K^{(\omega_0)}}{\partial t^2} = -\frac{3\epsilon_0 \mu_0 \chi^{(3)}}{8} \omega_0^2 (E_0|E_0|^2 + 2E_0|E_1|^2 + 2E_0|E_{-1}|^2) e^{i(k_0z - \omega_0t)}, \quad (29)$$

$$\mu_0 \frac{\partial^2 P_K^{(\omega_1)}}{\partial t^2} = -\frac{3\epsilon_0 \mu_0 \chi^{(3)}}{8} \omega_1^2 (E_1|E_1|^2 + 2E_1|E_0|^2 + 2E_1|E_{-1}|^2) e^{i(k_1z - \omega_1t)}. \quad (30)$$

In addition, because

$$\omega_0 - \omega_{-1} = \omega_1 - \omega_0 = \omega_v, \quad (31)$$

$$\omega_1 + \omega_{-1} - 2\omega_0 = 0, \quad (32)$$

$P_K^{(2\omega_0 - \omega_1)}$ ,  $P_K^{(\omega_1 + \omega_{-1} - \omega_0)}$ , and  $P_K^{(2\omega_0 - \omega_1)}$  are resonant to  $\omega_{-1}$ ,  $\omega_0$ , and  $\omega_1$ , respectively, and with the addition of  $\mu_0$  their second-order time derivatives are of the form

$$\begin{aligned} \mu_0 \frac{\partial^2 P_K^{(2\omega_0 - \omega_1)}}{\partial t^2} &= -\frac{3\epsilon_0 \mu_0 \chi^{(3)}}{8} (2\omega_0 - \omega_1)^2 E_0^2 E_1^* e^{i[(2k_0 - k_1)z - (2\omega_0 - \omega_1)t]} \\ &= -\frac{3\epsilon_0 \mu_0 \chi^{(3)}}{8} \omega_{-1}^2 E_0^2 E_1^* e^{i[(2k_0 - k_1)z - \omega_{-1}t]}, \end{aligned} \quad (33)$$

$$\begin{aligned} \mu_0 \frac{\partial^2 P_K^{(\omega_1 + \omega_{-1} - \omega_0)}}{\partial t^2} &= -\frac{6\epsilon_0 \mu_0 \chi^{(3)}}{8} (\omega_1 + \omega_{-1} - \omega_0)^2 \\ &\quad \times E_1 E_{-1} E_0^* e^{i[(k_1 + k_{-1} - k_0)z - (\omega_1 + \omega_{-1} - \omega_0)t]} \\ &= -\frac{6\epsilon_0 \mu_0 \chi^{(3)}}{8} \omega_0^2 E_1 E_{-1} E_0^* e^{i[(k_1 + k_{-1} - k_0)z - \omega_0 t]}, \end{aligned} \quad (34)$$

$$\begin{aligned} \mu_0 \frac{\partial^2 P_K^{(2\omega_0 - \omega_1)}}{\partial t^2} &= -\frac{3\epsilon_0 \mu_0 \chi^{(3)}}{8} (2\omega_0 - \omega_{-1})^2 \\ &\quad \times E_0^2 E_{-1}^* e^{i[(2k_0 - k_{-1})z - (2\omega_0 - \omega_{-1})t]} \\ &= -\frac{3\epsilon_0 \mu_0 \chi^{(3)}}{8} \omega_1^2 E_0^2 E_{-1}^* e^{i[(2k_0 - k_{-1})z - \omega_1 t]}, \end{aligned} \quad (35)$$

where Eq. (32) is used.

#### D. Full coupled equations with the Raman and Kerr terms

To complete building full coupled equations containing the Raman and Kerr effects, we insert the Raman terms [Eqs. (15)–(17)] and the Kerr terms [Eqs. (28)–(30) and (33)–(35)] into the right-hand side of Eq. (2) and also insert Eqs. (10) and (11) into the left-hand side of Eq. (2). Using resonant terms for each  $\omega_j$  ( $j = -1, 0, 1$ ), we obtain the following coupled equations:

$$\begin{aligned} \frac{\partial E_{-1}}{\partial z} &= i \frac{g}{2} q^* E_0 e^{i\Delta k_0 z} + i\kappa_{-1} (2|E_0|^2 + |E_{-1}|^2 + 2|E_1|^2) \\ &\quad \times E_{-1} + i\kappa_{-1} E_1^* E_0^2 e^{i\Delta k z}, \end{aligned} \quad (36)$$

$$\begin{aligned} \frac{\partial E_0}{\partial z} &= i \frac{g}{2} \frac{\omega_0}{\omega_{-1}} (q E_{-1} e^{-i\Delta k_0 z} + q^* E_1 e^{i\Delta k_1 z}) \\ &\quad + i\kappa_0 (|E_0|^2 + 2|E_{-1}|^2 + 2|E_1|^2) E_0 \\ &\quad + 2i\kappa_0 E_0^* E_{-1} E_1 e^{-i\Delta k z}, \end{aligned} \quad (37)$$

$$\begin{aligned} \frac{\partial E_1}{\partial z} &= i \frac{g}{2} \frac{\omega_1}{\omega_{-1}} q E_0 e^{-i\Delta k_1 z} + i\kappa_1 (2|E_0|^2 + 2|E_{-1}|^2 + |E_1|^2) \\ &\quad \times E_1 + i\kappa_1 E_{-1}^* E_0^2 e^{i\Delta k z}, \end{aligned} \quad (38)$$

$$\frac{\partial q}{\partial t} = \frac{1}{\tau} [-q + i(E_0 E_{-1}^* e^{i\Delta k_0 z} + E_1 E_0^* e^{i\Delta k_1 z})], \quad (39)$$

where Eq. (39) is used to determine the motion of  $q$  in Eqs. (36)–(38), which is given from Eq. (25). Equations (36)–(39) are already rewritten by our using the following quantities:

$$E_{\text{new}} = \left( \frac{\epsilon_0 c n}{2} \right)^{1/2} E_{\text{old}}, \quad (40)$$

$$q_{\text{new}} = \frac{2\omega_v \epsilon_0 c n}{\tau \gamma} q_{\text{old}}, \quad (41)$$

$$g = \frac{\omega_{-1} \tau \gamma}{4n^2 \epsilon_0 c^2 \omega_v} \chi^{(3)}, \quad (42)$$

$$\kappa_j = \frac{\omega_j}{c} n_2, \quad (43)$$

$$n_2 = \frac{3}{4c n^2 \epsilon_0} \chi^{(3)}, \quad (44)$$

$$\Delta k_j = k_j - k_{j-1} - k_v, \quad (45)$$

$$\Delta k = 2k_0 - k_1 - k_{-1}, \quad (46)$$

where  $g$  in Eq. (42) is the Raman gain,  $n_2$  in Eq. (44) is the nonlinear refractive index, and  $k_i$  ( $i = -1, 0, 1$ ) in Eq. (46) is given as  $k_i = \mathbf{k}_i \cdot \mathbf{z}$ , where  $\mathbf{k}_i \parallel \hat{\mathbf{z}}$  and  $\hat{\mathbf{z}}$  is a unit vector in

the  $z$  direction.

At the steady state, vibrating molecules with frequency  $\omega_v$  in the semiconductor used have a constant amplitude for  $q$  in the motion of  $Q = [qe^{i(k_v z - \omega_v t)} + \text{c.c.}]/2$ . Thus, the relation  $\partial q/\partial t = 0$  holds, and Eq. (39) gives

$$q = i(E_0 E_{-1}^* e^{i\Delta k_0 z} + E_1 E_0^* e^{i\Delta k_1 z}). \quad (47)$$

In this case, substituting Eq. (47) into Eqs. (36)–(38), we obtain

$$\begin{aligned} \frac{\partial E_{-1}}{\partial z} &= \frac{g}{2} (E_0^* E_{-1} + E_1^* E_0 e^{i\Delta k z}) E_0 \\ &+ i\kappa_{-1} (2|E_0|^2 + |E_{-1}|^2 + 2|E_1|^2) E_{-1} \\ &+ i\kappa_{-1} E_1^* E_0^2 e^{i\Delta k z}, \end{aligned} \quad (48)$$

$$\begin{aligned} \frac{\partial E_0}{\partial z} &= \frac{g}{2} \frac{\omega_0}{\omega_{-1}} (|E_1|^2 - |E_{-1}|^2) E_0 \\ &+ i\kappa_0 (|E_0|^2 + 2|E_{-1}|^2 + 2|E_1|^2) E_0 \\ &+ 2i\kappa_0 E_0^* E_{-1} E_1 e^{-i\Delta k z}, \end{aligned} \quad (49)$$

$$\begin{aligned} \frac{\partial E_1}{\partial z} &= -\frac{g}{2} \frac{\omega_1}{\omega_{-1}} (E_0 E_{-1}^* e^{i\Delta k z} + E_1 E_0^*) E_0 \\ &+ i\kappa_1 (2|E_0|^2 + 2|E_{-1}|^2 + |E_1|^2) E_1 \\ &+ i\kappa_1 E_{-1}^* E_0^2 e^{i\Delta k z}. \end{aligned} \quad (50)$$

If we include linear-loss terms with loss coefficient  $\alpha_j$  ( $j = -1, 0, 1$ ) and nonlinear-loss terms with TPA coefficient  $\beta_{\text{TPA}}$ , the coupled equations take the form

$$\begin{aligned} \frac{\partial E_{-1}}{\partial z} &= \frac{g}{2} (E_0^* E_{-1} + E_1^* E_0 e^{i\Delta k z}) E_0 \\ &+ i\kappa_{-1} (2|E_0|^2 + |E_{-1}|^2 + 2|E_1|^2) E_{-1} \\ &+ i\kappa_{-1} E_1^* E_0^2 e^{i\Delta k z} - \frac{1}{2} (\alpha_{-1} + \alpha_{-1}^{\text{TPA}}) E_{-1}, \end{aligned} \quad (51)$$

$$\begin{aligned} \frac{\partial E_0}{\partial z} &= \frac{g}{2} \frac{\omega_0}{\omega_{-1}} (|E_1|^2 - |E_{-1}|^2) E_0 \\ &+ i\kappa_0 (|E_0|^2 + 2|E_{-1}|^2 + 2|E_1|^2) E_0 \\ &+ 2i\kappa_0 E_0^* E_{-1} E_1 e^{-i\Delta k z} - \frac{1}{2} (\alpha_0 + \alpha_0^{\text{TPA}}) E_0, \end{aligned} \quad (52)$$

$$\begin{aligned} \frac{\partial E_1}{\partial z} &= -\frac{g}{2} \frac{\omega_1}{\omega_{-1}} (E_0 E_{-1}^* e^{i\Delta k z} + E_1 E_0^*) E_0 \\ &+ i\kappa_1 (2|E_0|^2 + 2|E_{-1}|^2 + |E_1|^2) E_1 \\ &+ i\kappa_1 E_{-1}^* E_0^2 e^{i\Delta k z} - \frac{1}{2} (\alpha_1 + \alpha_1^{\text{TPA}}) E_1, \end{aligned} \quad (53)$$

where  $\alpha_j^{\text{TPA}}$  is defined by [28,33]

$$\alpha_j^{\text{TPA}} = \beta_{\text{TPA}} \left( |E_j|^2 + 2 \sum_{m \neq j} |E_m|^2 \right), \quad (54)$$

and  $\beta_{\text{TPA}}$  is defined by

$$\beta_{\text{TPA}} = \frac{3\mu_0 \omega_j}{2n^2} \chi^{(3)}. \quad (55)$$

In the above equations, FCA is ignored because the  $p$ - $n$  junction in Fig. 1 soon drains off TPA-induced carriers (if there is TPA).

The right-hand sides of Eqs. (51)–(53) contain the terms for SRS, SPM, XPM, FWM (degenerate FWM), linear loss, and TPA loss from the left to the right. The SPM, XPM, and FWM terms are not negligible because the nonlinear coefficient  $\kappa_j$  in Eqs. (51)–(53) is comparable to the Raman gain  $g$  for  $\text{Al}_x\text{Ga}_{1-x}\text{As}$  at around  $1.55 \mu\text{m}$ :  $g \approx 10 \text{ cm/GW}$  [16] and  $\kappa_j \approx 7.1 \text{ cm/GW}$  [34]. For comparison, for Si at around  $1.55 \mu\text{m}$ ,  $g \approx 20 \text{ cm/GW}$  [4] and  $\kappa_j \approx 1.8 \text{ cm/GW}$  [35]. For Si, the effect from the SRS terms is much stronger than that from the Kerr terms, which is completely different from the  $\text{Al}_x\text{Ga}_{1-x}\text{As}$  case.

In the next section, we solve Eqs. (51)–(53) by an analytical method with some approximations and also by a numerical method when there is no QPM structure. After checking numerical solutions at the initial evolution stage by comparison with analytical solutions, we proceed to numerically obtain the output efficiency with the QPM structure out of the initial stage.

In what follows,  $|E_i|^2$  ( $i = -1, 0, 1$ ) represents the optical intensity in the unit of gigawatts per square centimeter, which is identical to the propagating beam power divided by the waveguide cross-section area.

## IV. RESULTS AND DISCUSSION

### A. Analytical solutions with approximations

To obtain analytical solutions for the coupled nonlinear equations [Eqs. (51)–(53)], we make the following approximations, which are valid at the initial stage of growth of the Stokes and anti-Stokes waves:

(1) The pump intensity  $|E_0|^2$  is sufficiently large compared with the intensities  $|E_{-1}|^2$ ,  $|E_1|^2$  of the Stokes and anti-Stokes waves, respectively, where the depletion of the pump beam is ignored. In this case, the condition

$$|E_{-1}|, |E_1| \ll |E_0| = \text{constant} \quad (56)$$

holds. The Stokes and anti-Stokes waves can grow from small seed light and do not necessarily require high-power seed beams at  $z = 0$ .



(2) Since the anti-Stokes wave with a phase mismatch  $\Delta k$  grows much more weakly than the Stokes wave with no such phase mismatch, the additional approximation

$$|E_1| \ll |E_{-1}| \quad (57)$$

holds.

(3) We ignore the wavelength dependence of the loss coefficients  $\alpha_{-1}$ ,  $\alpha_1$ , and  $\alpha_0$  of the Stokes, anti-Stokes, and pump waves, respectively, because their differences are small at wavelengths far from the band-gap wavelength (actually they are near the half-band-gap wavelength). In this case, we can set

$$\alpha_{-1} \approx \alpha_1 \approx \alpha_0 \equiv \alpha, \quad (58)$$

where  $\alpha$  is a constant.

Using Eqs. (56)–(58), we obtain the following simplified equations for Eqs. (51)–(53):

$$\frac{\partial E_{-1}}{\partial z} \approx \left( \frac{g}{2} - \beta_{\text{TPA}} + 2i\kappa_{-1} \right) |E_0|^2 E_{-1} - \frac{\alpha}{2} E_{-1}, \quad (59)$$

$$\frac{\partial E_1}{\partial z} \approx - \left( \frac{g}{2} \frac{\omega_1}{\omega_{-1}} - i\kappa_1 \right) E_0^2 E_{-1}^* e^{i\Delta k z} - \frac{\alpha}{2} E_1. \quad (60)$$

In the approximations used above, the effects of SPM and XPM are greatly reduced. (These effects are examined in detail in Sec. IV B 4.)

In Eqs. (59) and (60), the linear-loss terms are easily removed by our setting

$$E_{-1} = \mathcal{E}_{-1}(z) e^{-\frac{\alpha}{2}z}, \quad (61)$$

$$E_1 = \mathcal{E}_1(z) e^{-\frac{\alpha}{2}z}. \quad (62)$$

We then obtain

$$\frac{\partial \mathcal{E}_{-1}}{\partial z} \approx \left( \frac{g}{2} - \beta_{\text{TPA}} + 2i\kappa_{-1} \right) |E_0|^2 \mathcal{E}_{-1}, \quad (63)$$

$$\frac{\partial \mathcal{E}_1}{\partial z} \approx - \left( \frac{g}{2} \frac{\omega_1}{\omega_{-1}} - i\kappa_1 \right) E_0^2 \mathcal{E}_{-1}^* e^{i\Delta k z}. \quad (64)$$

To solve Eqs. (63) and (64), we integrate Eq. (63) from 0 to  $z$  and get

$$\mathcal{E}_{-1}(z) = \mathcal{E}_{-1}(0) e^{(g/2 - \beta_{\text{TPA}} + 2i\kappa_{-1})|E_0|^2 z}. \quad (65)$$

Next, inserting Eq. (65) into Eq. (64) and integrating Eq. (64) from 0 to  $z$ , we obtain

$$\begin{aligned} \mathcal{E}_1(z) = & \mathcal{E}_1(0) + \left( \frac{g}{2} \frac{\omega_1}{\omega_{-1}} - i\kappa_1 \right) E_0^2 \mathcal{E}_{-1}^*(0) \\ & \times \frac{1 - e^{[(\frac{g}{2} - \beta_{\text{TPA}})|E_0|^2 + i(\Delta k - 2\kappa_{-1}|E_0|^2)]z}}{(\frac{g}{2} - \beta_{\text{TPA}})|E_0|^2 + i(\Delta k - 2\kappa_{-1}|E_0|^2)}, \end{aligned} \quad (66)$$

where  $\mathcal{E}_1(0)$  denotes the input electric field for the anti-Stokes wave. In what follows, we set  $\mathcal{E}_1(0) \approx 0$  as  $\mathcal{E}_1(0)$  is a very small quantity.

Finally, substituting Eqs. (65) and (66) into Eqs. (61) and (62), we obtain

$$E_{-1}(z) = E_{-1}(0) e^{[(\frac{g}{2} - \beta_{\text{TPA}} + 2i\kappa_{-1})|E_0|^2 - \frac{\alpha}{2}]z}, \quad (67)$$

$$\begin{aligned} E_1(z) = & \left( \frac{g}{2} \frac{\omega_1}{\omega_{-1}} - i\kappa_1 \right) E_0^2 E_{-1}^*(0) e^{-(\alpha/2)z} \\ & \times \frac{1 - e^{[(g/2 - \beta_{\text{TPA}})|E_0|^2 + i(\Delta k - 2\kappa_{-1}|E_0|^2)]z}}{(g/2 - \beta_{\text{TPA}})|E_0|^2 + i(\Delta k - 2\kappa_{-1}|E_0|^2)}, \end{aligned} \quad (68)$$

where the relations  $E_1(0) = \mathcal{E}_1(0)$  and  $E_{-1}(0) = \mathcal{E}_{-1}(0)$  are used. From Eqs. (67) and (68), the output efficiencies,  $\eta_S = |E_{-1}(z)|^2/|E_0|^2$ ,  $\eta_{AS} = |E_1(z)|^2/|E_0|^2$  (i.e., the  $z$ -dependent Stokes and anti-Stokes intensities,  $|E_{-1}(z)|^2$ ,  $|E_1(z)|^2$ , divided by the initial pump intensity  $|E_0(0)|^2 = |E_0|^2$ ) are given as follows:

$$\eta_S = \frac{|E_{-1}(0)|^2}{|E_0|^2} e^{[(g - 2\beta_{\text{TPA}})|E_0|^2 - \alpha]z}, \quad (69)$$

$$\eta_{AS} = \left( \frac{g^2}{4} \frac{\omega_1^2}{\omega_{-1}^2} + \kappa_1^2 \right) |E_0|^2 |E_{-1}(0)|^2 e^{-\alpha z} \frac{1 - 2 \cos [(\Delta k - 2\kappa_{-1}|E_0|^2)z] e^{(g/2 - \beta_{\text{TPA}})|E_0|^2 z} + e^{(g - 2\beta_{\text{TPA}})|E_0|^2 z}}{(g/2 - \beta_{\text{TPA}})^2 |E_0|^4 + (\Delta k - 2\kappa_{-1}|E_0|^2)^2}. \quad (70)$$

From Eqs. (69) and (70), we can see some properties of the evolution of the Stokes and anti-Stokes waves:

(1) SRS and TPA for both Stokes and anti-Stokes waves in Eqs. (69) and (70) have the same dependence on the pump intensity  $|E_0|^2$ , which originates from the property

that their coefficients  $g$ ,  $\beta_{\text{TPA}}$  have the same origin of  $\chi^{(3)}$ , as seen in Eqs. (42) and (55), and have the same unit (cm/GW).

(2) In addition to the linear optical loss ( $e^{-\alpha z}$ ), SRS for the Stokes wave is suppressed by TPA as  $e^{(g-2\beta_{\text{TPA}})|E_0|^2 z}$ , as seen in Eq. (69). For the anti-Stokes wave in Eq. (70), SRS with optical losses is seemingly complicated because of the presence of  $\Delta k$  in Eq. (70). But the basic feature is that, in addition to the linear loss ( $e^{-\alpha z}$ ), SRS with  $e^{g|E_0|^2 z}$  is suppressed by TPA with  $e^{-\beta_{\text{TPA}}|E_0|^2 z}$ , resulting in  $e^{(g-2\beta_{\text{TPA}})|E_0|^2 z}$  and  $e^{(g/2-\beta_{\text{TPA}})|E_0|^2 z}$ .

(3) The output efficiency of the anti-Stokes wave in Eq. (70) oscillates with a period of  $\Lambda' = 2\pi/|\Delta k - 2\kappa_{-1}|E_0|^2|$ , which depends on  $2\kappa_{-1}|E_0|^2$ . Thus, the period has an  $|E_0|^2$  dependence.

(4) The output efficiency of the anti-Stokes wave in Eq. (70) is enhanced by an additional factor  $\kappa_1^2$  that stems from FWM, which is added to the SRS factor  $(g^2/4)(\omega_1^2/\omega_{-1}^2)$ .

As regards (1), since  $g$  and  $\beta_{\text{TPA}}$  are proportional to  $\chi^{(3)}$ , as seen in Eqs. (42) and (55), and since  $n_2$  is proportional to  $\chi^{(3)}$ , as seen in Eq. (44), these coefficients in the intermixed domains are smaller than those in the as-grown domains because of blueshifted resonance for  $\chi^{(3)}$  and  $\chi^{(3)}$ . Thus, periodic  $g$  and  $n_2$  are produced in the GaAs/AlAs-intermixed-superlattice waveguide. These periodic  $g$  and  $n_2$  form the QPM structure that can remove  $\Delta k$  and enhance the output efficiency.

In connection with (2), if the photon energies of the Stokes and anti-Stokes waves are smaller than the half-band-gap energy, TPA that degrades SRS can be greatly reduced. Even in this region,  $n_2$  has a finite value (and becomes large near the half-band-gap energy) [29]. For this reason, we use a semiconductor device with the photon energies of the pump, Stokes, and anti-Stokes waves near and below the half-band-gap energy for highly efficient output (or with their wavelengths near and greater than the half-band-gap wavelength).

In relation to (3), the setting of the QPM period  $\Lambda$  to  $\Lambda' = 2\pi/|\Delta k - 2\kappa_{-1}|E_0|^2|$  is not practical in device applications because  $|E_0|^2$  decreases as the pump wave propagates through the QPM device, as shown in Sec. IV B, which requires an aperiodic QPM structure. In addition,  $|E_0|^2$  at  $z = 0$  is sometimes varied, and a corresponding aperiodic QPM structure is necessary in this case. This means that there is no tolerance of a wide change in input pump intensity. For this reason, we set  $\Lambda = 2\pi/|\Delta k|$  when performing quasi-phase-matching.

With regard to (4), because  $\kappa_1^2 \approx 50.4$  and  $(g^2/4)(\omega_1^2/\omega_{-1}^2) \approx 29.9$  in our case, we can see that the FWM-enhanced efficiency is about 2.7 times greater than the efficiency without FWM. For comparison, we mention that Si has  $\kappa_1^2 \approx 3.3$  and  $(g^2/4)(\omega_1^2/\omega_{-1}^2) \approx 119.6$ , which

means that Si has a little efficiency enhancement by FWM. On the other hand, such enhancement has been reported in an optical fiber (SiO<sub>2</sub>) with no QPM structure [36]. However, our device has a QPM structure, and we need to investigate the effect of SRS with FWM in the QPM structure. At the same time, we need to take account of SPM and XPM, which are much stronger than in SiO<sub>2</sub> as well as in Si. The numerical analysis containing all those effects on the efficiency is given in the next section.

## B. Numerical solutions

The solutions in Sec. IV A with approximations for nonlinear optical terms do not contain the effects of pump depletion and very large growth of the Stokes wave under the assumption that they are at the initial stage. To investigate the evolution of the three waves more precisely, we obtain numerical solutions (i.e., without such approximations) for the case without the QPM structure first by the fourth-order Runge-Kutta method [37]. At the initial wave evolution, since those two effects are not serious, a comparison between the analytical and numerical solutions can be made to check numerical accuracy, which is described in Sec. IV B 4. After this check, we investigate the solutions for the QPM case, and show improved output characteristics in comparison with the no-QPM case.

### 1. Determination of the half-band-gap, Stokes, pump, and anti-Stokes wavelengths

We use Al<sub>x</sub>Ga<sub>1-x</sub>As ( $x = 0.18$ ), where the  $\chi^{(3)}$  property of the as-grown GaAs/AlAs superlattice can be well approximated. The Al<sub>x</sub>Ga<sub>1-x</sub>As ( $x = 0.18$ ) and the GaAs/AlAs superlattice have a quite similar  $\chi^{(3)}$  property and almost the same band-gap energy [29]. We do not have to focus on TPA in the intermixed regions because they have a blueshifted absorption edge, and TPA in the as-grown regions emerges first. In this superlattice, we assume that the Stokes, pump, and anti-Stokes wavelengths,  $\lambda_i$  ( $i = -1, 0, 1$ ), respectively, are near and greater than the half-band-gap wavelength  $\lambda_{\text{half}}$ , thus keeping large  $n_2$  and very small (almost zero)  $\beta_{\text{TPA}}$ . (Here a large figure of merit,  $4\pi n_2/(\beta_{\text{TPA}}\lambda_i) \gg 1$ , is kept even at  $\lambda_i = \lambda_{\text{half}}$  [38,39].)

To show available  $\lambda_{-1}, \lambda_0, \lambda_1$ , we need to calculate  $\lambda_{\text{half}}$  ( $\mu\text{m}$ ), which is defined by

$$\lambda_{\text{half}} = 2 \frac{hc}{E_g}, \quad (71)$$

where  $h$  is Planck's constant,  $c$  is the velocity of light, and  $E_g$  (eV) is the band-gap energy at temperature  $T$  (K).  $E_g$  in Eq. (71) can be determined from Varshni's equation [40] for Al<sub>x</sub>Ga<sub>1-x</sub>As:

$$E_g = E_g^{(0)} - \frac{aT^2}{b + T}, \quad (72)$$

where  $E_g^{(0)} = (1.5194 + 1.36x + 0.22x^2)$  eV ( $0.1 < x < 0.75$ ) [41],  $a = (5.5 + 3.35x) \times 10^{-4}$  eV/K, and  $b = (225 + 88x)$  K ( $0 < x < 0.7$ ), which are valid for 12–800 K [42].

Setting  $x = 0.18$  and  $T = 300$  K (room temperature) in Eqs. (71) and (72), we obtain  $E_g = 1.67$  eV and  $\lambda_{\text{half}} = 1.485$   $\mu\text{m}$ . Thus, for  $\lambda_{-1}$ ,  $\lambda_0$ , and  $\lambda_1$  near and greater than  $\lambda_{\text{half}} = 1.485$   $\mu\text{m}$  (0.835 eV), we obtain  $\lambda_{-1} = 1.63$   $\mu\text{m}$  (0.761 eV),  $\lambda_0 = 1.56$   $\mu\text{m}$  (0.795 eV), and  $\lambda_1 = 1.49$   $\mu\text{m}$  (0.832 eV). Here the spacing of  $\lambda_{-1}$ ,  $\lambda_0$ ,  $\lambda_1$  is determined from the Raman shift (70.8 nm) of  $\text{Al}_x\text{Ga}_{1-x}\text{As}$ .

## 2. Determination of the phase mismatch $\Delta k$

It is also necessary to determine the phase mismatch  $\Delta k$  in Eqs. (51)–(53) when one is numerically integrating them.  $\Delta k$  is defined by

$$\begin{aligned} \Delta k &= 2k_0 - k_1 - k_{-1} \\ &= 2\pi \left[ 2 \frac{n(\lambda_0)}{\lambda_0} - \frac{n(\lambda_1)}{\lambda_1} - \frac{n(\lambda_{-1})}{\lambda_{-1}} \right], \end{aligned} \quad (73)$$

where  $n(\lambda_i)$  is the refractive index for  $\lambda_i$  ( $i = -1, 0, 1$ ). The form of  $n(\lambda_i)$  is determined by Sellmeier's equation for  $\text{Al}_x\text{Ga}_{1-x}\text{As}$  at room temperature [43,44], which is given by

$$n(\lambda_i) = \left[ a_1 - a_2x + \frac{a_3}{\lambda_i^2 - (a_4 - a_5x)^2} - a_6(a_7x + 1)\lambda_i^2 \right]^{\frac{1}{2}}, \quad (74)$$

where for  $x \leq 0.36$ ,  $a_1 = 10.906$ ,  $a_2 = 2.92$ ,  $a_3 = 0.97501$ ,  $a_4 = 0.52886$ ,  $a_5 = 0.735$ ,  $a_6 = 0.002467$ , and  $a_7 = 1.41$ . For  $x > 0.36$ ,  $a_4$  and  $a_5$  are changed to  $a_4 = 0.30386$  and  $a_5 = 0.105$ . Since Sellmeier's equation for the as-grown regions has not been obtained, although there have been some experimentally measured refractive indices at around 1.55  $\mu\text{m}$  [23], we use Eq. (74) with  $x = 0.18$  as an approximate refractive index for the as-grown regions. When compared with the experimentally measured refractive index at 1.55  $\mu\text{m}$  for TE modes [23], the deviation of the refractive index from that in Eq. (74) with  $x = 0.18$  at 1.55  $\mu\text{m}$  is 5.8%.

From Eqs. (73) and (74), we can determine the period  $\Lambda$  for first-order quasi-phase-matching as  $\Lambda = 2\pi/|\Delta k|$ . By inserting  $\lambda_{-1} = 1.63$   $\mu\text{m}$ ,  $\lambda_0 = 1.56$   $\mu\text{m}$ , and  $\lambda_1 = 1.49$   $\mu\text{m}$  into Eqs. (73) and (74), we obtain  $\Lambda = 189.1$   $\mu\text{m}$ .

## 3. Determination of the linear-loss coefficient $\alpha$

Since the Stokes, pump, and anti-Stokes wavelengths are greater than the half-band-gap wavelength, the TPA loss does not emerge, but the linear loss emerges at all

times. However, recent technological development has achieved a small linear loss; for example, a loss of 1.2 dB/cm in  $\text{Al}_x\text{Ga}_{1-x}\text{As}$  ( $x = 0.18$ ) at around 1.55  $\mu\text{m}$  for TE-mode beams [45]. We use this value in our calculations. In addition, since wavelengths greater than the half-band-gap wavelength are far from the band-gap wavelength, we can justify the omission of the wavelength dependence of the linear-loss coefficients  $\alpha_j$  ( $j = -1, 0, 1$ ), as given in Eq. (58), and we set  $\alpha_j = \alpha = 0.276$   $\text{cm}^{-1}$ . This is calculated from the loss of 1.2 dB/cm so as to fit  $e^{-\alpha z}$ .

## 4. Output efficiencies for the cases with and without the QPM structure

Using the phase mismatch  $\Delta k$ , the refractive indices  $n(\lambda_i)$  of the wavelengths  $\lambda_i$  ( $i = -1, 0, 1$ ), the linear-loss coefficient  $\alpha$ , and the numerical factors of  $g$  and  $\kappa_j$  given in Sec. III D, we numerically compute the output efficiencies,  $\eta_S = |E_{-1}(z)|^2/|E_0(0)|^2$ ,  $\eta_{AS} = |E_1(z)|^2/|E_0(0)|^2$ , for the cases with and without the QPM structure.

In numerical calculations with the QPM structure, the small difference between the refractive indices,  $n_{\text{intermixed}}$  and  $n_{\text{as-grown}}$ , in the intermixed and as-grown domains, respectively, is ignored because the difference  $n_{\text{as-grown}} - n_{\text{intermixed}} = 0.01$  is only 0.3% of the average refractive index of the QPM structure, as mentioned in Sec. I. On the other hand, a large change in  $\chi^{(3)}$  of the intermixed domains is set as  $\varepsilon\chi^{(3)}$  ( $0 \leq \varepsilon \leq 1$ ) using the  $\chi^{(3)}$  of the as-grown domains, as depicted in Fig. 3. This setting means that when  $\varepsilon = 1$ , there is no QPM structure and that when  $0 \leq \varepsilon < 1$ , there is a QPM structure. In particular,  $\varepsilon = 0$  gives a maximum QPM effect.

To calculate the output efficiencies, we use a waveguide with a cross-section area of  $(0.5$   $\mu\text{m})^2$  and a pump power of 10 W [46], which can be achieved with fiber lasers. In this case, the pump intensity at  $z = 0$  is  $|E_0(0)|^2 = 4.0$   $\text{GW}/\text{cm}^2$ . As seed-light intensities at  $z = 0$  for the Stokes and anti-Stokes waves, we tentatively set  $|E_{-1}(0)|^2 = 0.01$   $\text{GW}/\text{cm}^2$  and  $|E_1(0)|^2 = 0.0001$   $\text{GW}/\text{cm}^2$ . The setting of  $|E_{-1}(0)|^2 \approx |E_1(0)|^2 = 0.01$   $\text{GW}/\text{cm}^2$  is also possible. But we numerically check that within  $0.0001$   $\text{GW}/\text{cm}^2 \leq |E_1(0)|^2 \leq 0.01$   $\text{GW}/\text{cm}^2$

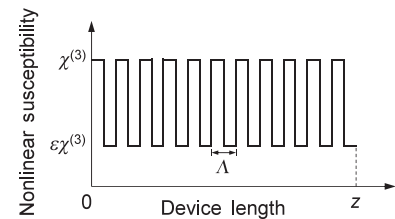


FIG. 3. Change in third-order nonlinear susceptibility  $\chi^{(3)}$  in the QPM structure.  $\chi^{(3)}$  in the intermixed domains is set to  $\varepsilon\chi^{(3)}$  with  $0 \leq \varepsilon \leq 1$ .  $\Lambda$  is the QPM period.

there is no noticeable change in the growth of the Stokes and anti-Stokes waves. We set  $|E_0(0)|^2 = 4.0 \text{ GW/cm}^2 \gg |E_{-1}(0)|^2 = 0.01 \text{ GW/cm}^2 \gg |E_1(0)|^2 = 0.0001 \text{ GW/cm}^2$  because this enables us to compare the numerical results with the analytical results obtained with the approximations in Eqs. (56) and (57).

The output efficiencies  $\eta_S, \eta_{AS}$  for  $\varepsilon = 1$  (i.e., without the QPM structure) as a function of the device length  $z$  are shown in Fig. 4, indicated by the red and blue curves, respectively. The pump intensity  $|E_0(z)|^2$  divided by  $|E_0(0)|^2$  is also included in Fig. 4, indicated by the green curve, which shows a rapid decrease with increasing  $z$ . The inset in Fig. 4 shows a magnification of the behavior of  $\eta_{AS}$  at around  $z = 0.15 \text{ cm}$ , which shows that  $\eta_{AS}$  oscillates and does not grow sufficiently due to a non-zero phase mismatch  $\Delta k$  and pump depletion. In this case, most of the pump power is transferred to the Stokes wave, which has no such phase mismatch.

From the inset in Fig. 4, we can roughly estimate the ratio,  $|E_1|^2/|E_{-1}|^2$ , between the anti-Stokes-wave and Stokes-wave intensities to be  $10^{-3}$ , which is rather larger than  $10^{-6} - 10^{-5}$  in Si waveguides [18,19]. This comes from  $|E_1|^2/|E_{-1}|^2$  being proportional to the pump intensity  $|E_0|^2$  [17] with the use of a larger  $|E_0|^2$  in our case.

As mentioned above, the input-intensity setting in numerical calculations that satisfies  $|E_0| \gg |E_{-1}| \gg |E_1|$  enables us to compare the numerical results with the analytical solutions in Eqs. (69) and (70) when  $\beta_{\text{TPA}} = 0$ . This is shown in Fig. 5, where the thin red and blue curves represent the analytical results from Eqs. (69) and (70), respectively, and the thick red, blue, and green curves are the same as in Fig. 4. The inset displays the same

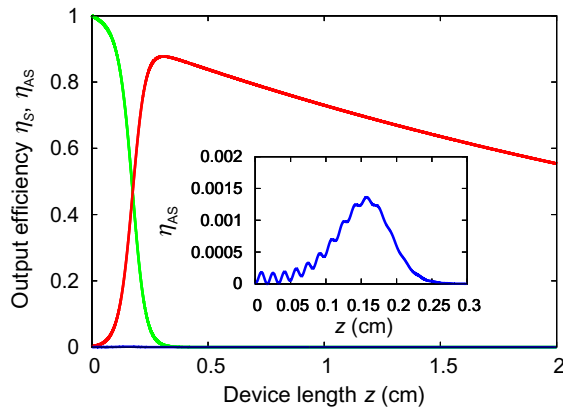


FIG. 4. Output efficiencies  $\eta_S = |E_{-1}(z)|^2/|E_0(0)|^2$  and  $\eta_{AS} = |E_1(z)|^2/|E_0(0)|^2$  of the Stokes and anti-Stokes waves, respectively, for  $\varepsilon = 1$  (i.e., without the QPM structure). The red and blue curves indicate  $\eta_S$  and  $\eta_{AS}$ , respectively, and the green curve indicates the normalized pump intensity  $|E_0(z)|^2/|E_0(0)|^2$ . The inset shows magnification of the behavior of  $\eta_{AS}$  at around 0.15 cm.

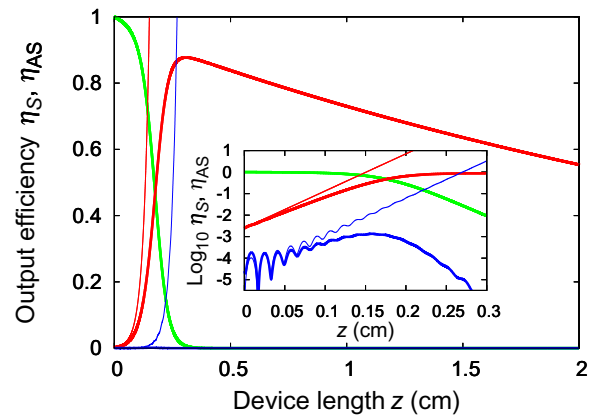


FIG. 5. Comparison between analytical and numerical results, indicated by the thin and thick curves, respectively, where the thick curves are the same as in Fig. 4. The inset shows the same plot with a  $\log_{10}$  scale for the vertical axis.

plot with a  $\log_{10}$  scale for the vertical axis. At the initial stage of growth of the Stokes and anti-Stokes waves, the numerical solutions well fit the analytical results, but that as  $z$  increases they deviate from the analytical results. The main cause of this is pump depletion, and there is also another effect from SPM and XPM, which are greatly reduced in the approximations for the analytical solutions. The latter effect is described below (see Fig. 7).

Figure 6 shows the output efficiencies  $\eta_S, \eta_{AS}$  for  $\varepsilon = 0$  (i.e., with the QPM structure that provides the maximum efficiency), where we observe a great increase in  $\eta_{AS}$  due to quasi-phase-matching, which reaches the same order of  $\eta_S$  (but with a factor of about 1/7). In addition, we can see that there is an optimal device length that provides the highest efficiency in  $\eta_{AS}$  at  $z_{\text{peak}} = 0.69 \text{ cm}$  that is determined from a balance between optical gain and loss. This gives us useful information for determining the necessary device length when we fabricate actual devices. In this case,  $\eta_S$  of

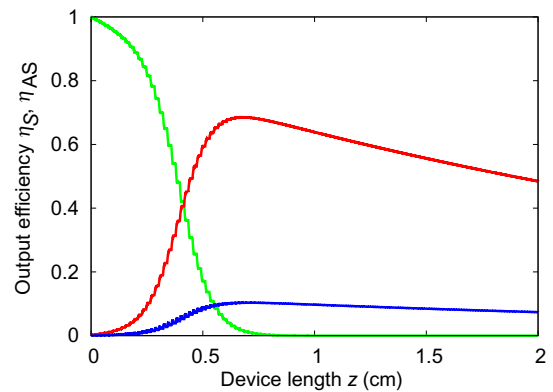


FIG. 6. Output efficiencies  $\eta_S$  and  $\eta_{AS}$  of the Stokes and anti-Stokes waves, respectively, for  $\varepsilon = 0$  (i.e., with the QPM structure giving the maximum efficiency). The red and blue curves show  $\eta_S$  and  $\eta_{AS}$ , respectively, and the green curve indicates the normalized pump intensity.



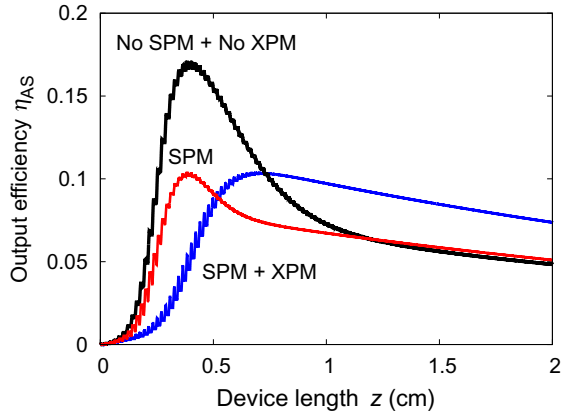


FIG. 7. Output efficiency  $\eta_{AS}$  without SPM and XPM, indicated by the black curve. The blue curve shows the case when SPM and XPM are included. The red curve indicates the case when only SPM is taken into account.

the Stokes wave somewhat decreases because more pump power is transferred to the anti-Stokes wave. We also check the influence of an initial phase shift (i.e., at  $z = 0$ ) of the QPM period on  $\eta_{AS}$ , and observe very little effect on it.

To check the effects of SPM and XPM on SRS of the anti-Stokes wave including FWM, we depict  $\eta_{AS}$  when SPM and/or XPM effects are deliberately deleted. The black curve in Fig. 7 depicts  $\eta_{AS}$  when only SRS and FWM are taken into account. The blue curve shows  $\eta_{AS}$  containing both SPM and XPM effects, which is the same as that in Fig. 6.

From the black curve, we can see that quasi-phase-matching is more effective because there is no period deviation from  $\Lambda = 2\pi/|\Delta k|$  by a phase shift due to SPM and XPM. Owing to this effective quasi-phase-matching,  $\eta_{AS}$  grows more rapidly than that with SPM and XPM as the anti-Stokes wave propagates in the  $z$  direction; in this case, about 1.6 times larger  $\eta_{AS}$  is obtained at  $z = 0.4$  cm.

Furthermore, to see only the SPM effect on  $\eta_{AS}$ , we intentionally delete the XPM effect, as depicted in Fig. 7 by the red curve. We can see that this also causes a period deviation from  $\Lambda = 2\pi/|\Delta k|$ , thus decreasing  $\eta_{AS}$ . But, in our semiconductor device, since we cannot remove only SPM and/or XPM effects in an artificial manner, the efficiency reduction in the device always occurs.

Next we check the dependence of  $\eta_{AS}$  on the  $\varepsilon$  ( $0 \leq \varepsilon \leq 1$ ) while taking account of all the above-mentioned nonlinear effects. Figure 8 shows the peak value of  $\eta_{AS}$  at  $z = z_{\text{peak}}$ , denoted by  $\eta_{AS,\text{peak}}$ , as a function of  $\varepsilon$ . In Fig. 8, we can see that as  $\varepsilon$  approaches 0 from 1,  $\eta_{AS,\text{peak}}$  increases rapidly. To obtain the QPM enhancement as compared with the no-QPM case (i.e.,  $\varepsilon = 1$ ), we calculate the enhancement factor  $e$  (or figure of merit) defined by

$$e = \frac{\eta_{AS,\text{peak},\varepsilon}}{\eta_{AS,\text{peak},\varepsilon=1}} = \frac{|E_1|_{\text{peak},\varepsilon}^2}{|E_1|_{\text{peak},\varepsilon=1}^2}. \quad (75)$$

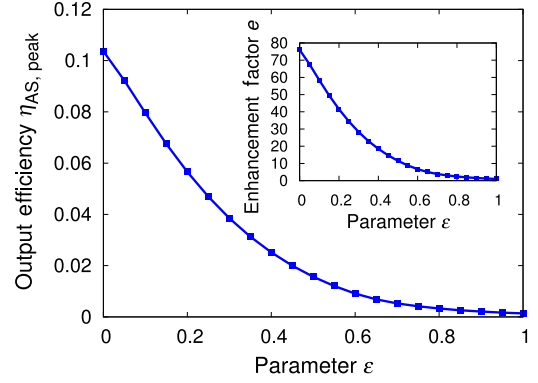


FIG. 8. Output efficiency  $\eta_{AS}$  at  $z = z_{\text{peak}}$  as a function of  $\varepsilon$  ( $0 \leq \varepsilon \leq 1$ ). The inset depicts the enhancement factor  $e$ .

This is depicted in the inset in Fig. 8, which shows that  $e$  is about 76 times greater at  $\varepsilon = 0$  (with the maximum QPM effect) than at  $\varepsilon = 1$  (with no QPM effect). Since the actually achievable value of  $\varepsilon$  is approximately 0.5 [29], the enhancement factor  $e$  in this case is approximately 11.5.

### 5. Dependence of QPM efficiency on the pump intensity

The enhancement factor  $e$  in the inset in Fig. 8 is obtained when the initial pump intensity  $|E_0(0)|^2$  is fixed at  $4.0 \text{ GW/cm}^2$ . As we can easily see, an increase in the initial pump intensity  $|E_0(0)|^2$  increases the anti-Stokes-wave intensity  $|E_1|_{\text{peak},\varepsilon}^2$ , which is shown in Fig. 9. Thus, our interest now turns to the dependence of  $e$  on  $|E_0(0)|^2$ .

The dependence of  $e$  on  $|E_0(0)|^2$  is depicted in the inset in Fig. 9, where the vertical axis has a  $\log_{10}$  scale. This shows that  $e$  has a very large value between  $10^3$  and  $10^{3.5}$  for  $0 \leq \varepsilon \leq 0.5$  at very small  $|E_0(0)|^2$ , where  $|E_0(0)|^2$  should be larger than the SRS threshold pump intensity  $\delta \approx 10^{-2} \text{ GW/cm}^2$  [47]. The increase in  $e$  occurs because as  $|E_0(0)|^2$  approaches  $\delta$ , the intensity-dependent period  $\Lambda' = 2\pi/|\Delta k - 2\kappa_{-1}|E_0|^2|$  in (3) of Sec. IV A that

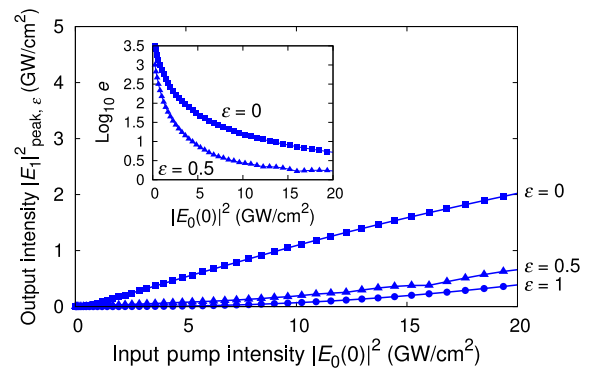


FIG. 9. Dependence of peak output intensity  $|E_1|_{\text{peak},\varepsilon}^2$  on the input pump intensity  $|E_0(0)|^2$  for  $\varepsilon = 0, 0.5$ , and  $1$ . The inset depicts a  $\log_{10}$  plot of the enhancement factor  $e$  versus  $|E_0(0)|^2$  when  $\varepsilon = 0$  or  $0.5$ .



page 10 comes nearer to  $\Lambda = 2\pi/|\Delta k|$ , thereby achieving highly-efficient QPM effect.  $\Lambda'$  will actually be affected by not only SPM but also XPM in the region beyond the approximations in Sec. IV A. But both SPM and XPM simultaneously diminish as  $|E_0(0)|^2$  approaches  $\delta$ , and thus the above simple interpretation holds in explaining the  $e$  enhancement.

For a comparison, in the perfectly-phase-matched case (i.e.,  $\Delta k = 0$ ), we can calculate the enhancement factor  $e' = \eta_{AS}(\Delta k = 0)/\eta_{AS}(\Delta k \neq 0)$  from Eq. (70) and obtain  $e' \gtrsim 5.9 \times 10^3 \approx 10^{3.77}$  for  $|E_0(0)|^2 \approx 0$  with  $z \gtrsim 0.35$  cm (where 0.35 cm appears because  $z_{\text{peak}} > 0.35$  cm at  $|E_0(0)|^2 < 4$  (GW/cm<sup>2</sup>) for  $\varepsilon \leq 0.5$ , as shown in Fig. 10). This estimation indicates that the above-mentioned  $e$  enhancement between  $10^3$  and  $10^{3.5}$  is very large and yet still smaller than that in the perfectly-phase-matched case.

### 6. Dependence of peak position on the pump intensity

In actual device fabrication, it is important to determine an optimal (i.e., the smallest) device length that gives the highest output intensity. Figure 10 depicts the dependence of the optimal device length  $z_{\text{peak}}$  on the pump intensity  $|E_0(0)|^2$ , which shows that  $z_{\text{peak}}$  decreases as  $|E_0(0)|^2$  increases. This is because as  $|E_0(0)|^2$  increases, the Stokes and anti-Stokes waves grow rapidly, thus causing rapid pump depletion. After complete pump depletion, the Stokes and anti-Stokes waves do not grow and are attenuated by the linear optical loss. Thus  $z = z_{\text{peak}}$  is given approximately from the complete-pump-depletion point.

The important information obtained from Fig. 10 is that we can determine the lower limit of an input pump intensity  $|E_0(0)|^2$  for the optimal waveguide length; For instance, as shown in the inset of Fig. 10 by the dashed line for  $\varepsilon = 0.5$ ,  $|E_0(0)|^2 = 1.2$  (GW/cm<sup>2</sup>) is necessary such that  $z_{\text{peak}} = 1$  (cm) that is the length aiming to actual device fabrication.

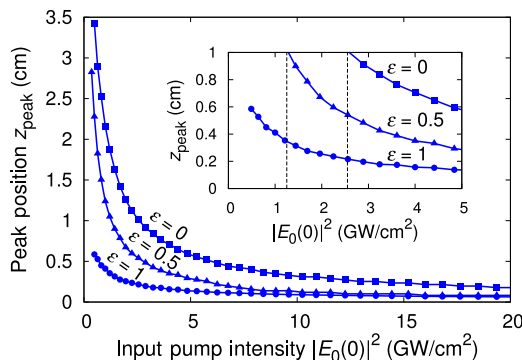


FIG. 10. Dependence of the peak position  $z_{\text{peak}}$  on the input pump intensity  $|E_0(0)|^2$  for  $\varepsilon = 0, 0.5$ , and 1. The inset shows a magnification for the ranges  $0 \leq z_{\text{peak}} \leq 1$  (cm) and  $0 < |E_0(0)|^2 < 5$  (GW/cm<sup>2</sup>). The dashed lines indicate the necessary  $|E_0(0)|^2$  for  $z_{\text{peak}} = 1$  cm when  $\varepsilon = 0$  or 0.5.

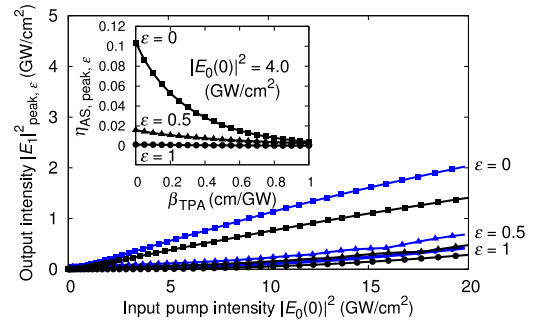


FIG. 11. Dependence on the input pump intensity  $|E_0(0)|^2$  of the peak output intensity  $|E_1|^2_{\text{peak},\varepsilon}$  of the anti-Stokes wave for  $\varepsilon = 0, 0.5$ , and 1 with  $\beta_{\text{TPA}} = 0.1$  cm/GW, indicated by the black curves, and with  $\beta_{\text{TPA}} = 0$  (cm/GW), indicated by the blue curves. The inset shows the  $|E_0(0)|^2$  dependence of the efficiency  $\eta_{AS,\text{peak},\varepsilon} = |E_1|^2_{\text{peak},\varepsilon}/|E_0(0)|^2$  when  $\beta_{\text{TPA}}$  is varied from 0 to 1 cm/GW.

### 7. Dependence of output efficiency on TPA

In Sec. IV B 1, since the Stokes, pump, and anti-Stokes wavelengths,  $\lambda_i$  ( $i = -1, 0, 1$ ), respectively, are near and greater than the half-band-gap wavelength,  $\lambda_{\text{half}}$ , sizable  $n_2$  and negligibly small  $\beta_{\text{TPA}}$  are obtained (i.e., high nonlinear refraction and very small TPA). But, in the case of  $\lambda_i$  ( $i = -1, 0, 1$ ) less than  $\lambda_{\text{half}}$ , TPA will emerge strongly. We examine this effect on the output efficiency.

TPA excites carriers, which give rise to FCA (i.e., an additional optical absorption). But we can remove this additional absorption by use of the reversed-biased  $p$ - $n$  junction in Fig. 1.

A detailed calculation containing FCA (e.g., in a Si waveguide) shows a remarkable increase in the optical losses of propagating beams with increasing input beam power; that is, the influence of FCA is far greater than that of only TPA [48]. Thus, the removal of TPA-induced carriers is indispensable for device applications.

Here, without including FCA with the help of the  $p$ - $n$  junction, we discuss the effect of TPA on the peak value  $|E_1|^2_{\text{peak},\varepsilon}$  at  $z = z_{\text{peak}}$  for  $\varepsilon = 0, 0.5$ , and 1. This is shown in Fig. 11 with use of  $\beta_{\text{TPA}} = 0.1$  cm/GW measured for TE modes [49], where the black curves depict  $|E_1|^2_{\text{peak},\varepsilon}$  with  $\beta_{\text{TPA}} = 0.1$  cm/GW and the blue curves show  $|E_1|^2_{\text{peak},\varepsilon}$  with  $\beta_{\text{TPA}} = 0$  cm/GW for comparison. In Fig. 11, we can see that the decrease in  $|E_1|^2_{\text{peak},\varepsilon}$  due to non-zero  $\beta_{\text{TPA}}$  becomes larger for smaller  $\varepsilon$ , where for smaller  $\varepsilon$ , the anti-Stokes-wave intensity is larger and thus there is stronger TPA.

In the inset in Fig. 11, we plot the peak output efficiency  $\eta_{AS,\text{peak},\varepsilon} = |E_1|^2_{\text{peak},\varepsilon}/|E_0(0)|^2$  for some different  $\beta_{\text{TPA}}$  values between 0 and 1 cm/GW when  $|E_0(0)|^2 = 4.0$  GW/cm<sup>2</sup>, because a value of  $\beta_{\text{TPA}}$  (0.35 cm/GW) different from 0.1 cm/GW has been reported [34]. In the inset, we observe that  $\eta_{AS,\text{peak},\varepsilon}$  decreases rapidly with increasing

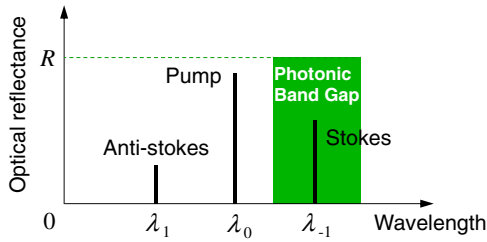


FIG. 12. Optical reflectance for dielectric multilayer mirrors or photonic crystals (with  $0 < R < 1$  by controlling the thickness of the dielectric multilayer mirrors or photonic crystals) that form a cavity, where they reflect the Stokes waves back to the device with their band gap and let the pump and anti-Stokes waves go through them. By this method, the enhancement in the Stokes-wave intensity  $|E_{-1}|^2$  provides high anti-Stokes efficiency  $\eta_{AS}$  because of  $\eta_{AS} \propto |E_{-1}|^2$ .

$\beta_{TPA}$ , where the decrease is more rapid for smaller  $\varepsilon$  because of stronger TPA with larger  $|E_1|_{\text{peak},\varepsilon}^2$ .

In the above, a great decrease in the output efficiency  $\eta_{AS}$  due to TPA has been shown quantitatively, and we recognize the significance of keeping  $\lambda_i$  ( $i = -1, 0, 1$ ) near and greater than  $\lambda_{\text{half}}$  to avoid TPA and obtain highly-efficient output for device applications.

In addition to this, to obtain much larger  $\eta_{AS}$ , we propose a cavity structure with dielectric multilayer mirrors or photonic crystals [50–54] attached to both ends of the device, which can also shorten the device. The dielectric multilayer mirrors and photonic crystals reflect the Stokes waves back to the device with their band gap with optical reflectance  $R$  to enhance the Stokes-wave intensity  $|E_{-1}|^2$  in the device and let the pump and anti-Stokes waves pass through them, as illustrated in Fig. 12. This enhancement in  $|E_{-1}|^2$  increases  $\eta_{AS}$  (with no necessity of boosting the pump intensity  $|E_0|^2$ ) owing to the relation  $\eta_{AS} \propto |E_{-1}|^2$  in Eq. (70). If we use band-gap structures with  $R < 1$ , it is possible to adjust the sizes of  $\eta_{AS}$  and  $\eta_S$  (and to equalize them, if necessary). Quantitative analysis of such efficiency adjustments will be provided in a forthcoming paper.

## V. SUMMARY

We propose a superlattice SRS device design using a GaAs/AlAs intermixed superlattice with  $\chi^{(3)}$  nonlinearity that can boost the anti-Stokes-wave efficiency  $\eta_{AS}$  by quasi-phase-matching at  $1.49 \mu\text{m}$  to the same order as the Stokes-wave efficiency  $\eta_S$  at  $1.63 \mu\text{m}$  with the input of a  $1.56\text{-}\mu\text{m}$  pump beam, which could be used for channel amplification and/or conversion in gigabit-Ethernet passive optical networks and wavelength-division multiplexing systems.

In particular, having focused on the anti-Stokes-wave amplification, we compute  $\eta_{AS}$  including the effects of FWM, SPM, and XPM with coupled nonlinear equations for the interacting pump, Stokes, and anti-Stokes waves,

because those effects are much stronger than in Si and  $\text{SiO}_2$ .

The solutions by an analytical method with approximations and by a numerical method show good agreement at the initial stage of growth of the Stokes and anti-Stokes waves for the no-QPM case. The analytical solutions show that FWM enhances SRS, where the influence of SPM and XPM is greatly reduced in the approximations. The numerical calculations without such approximations reveal that the difference between the analytical and numerical solutions in the behavior out of the initial stage stems from pump depletion and the SPM and XPM effects. To obtain  $\eta_{AS}$  precisely, we numerically compute it for the cases with and without the QPM structure containing FWM, SPM, and XPM effects. A comparison between the two cases shows that the efficiency is 3 orders of magnitude greater with the QPM structure than without it for  $\varepsilon \leq 0.5$  for a small pump intensity. The mechanism is clearly shown in terms of nonlinear-optical analysis. A TPA effect on  $\eta_{AS}$  at the optimal length is also examined, which indicates the significance of TPA reduction for device applications. In addition, we propose the use of a photonic-band-gap cavity to obtain greater  $\eta_{AS}$  or to control the sizes of  $\eta_{AS}$  and  $\eta_S$ .

The proposed device has potential in ultrahigh-speed data processing/routing applications using channel conversion and amplification via instantaneous optical nonlinear interactions without any influence of carriers, or electron-hole pairs, that distort the waveforms of optical signals.

## ACKNOWLEDGMENTS

I.T. thanks the Koshiyama Science & Technology Foundation for financial support. S.S. thanks the Engineering and Physical Sciences Research Council (Standard Grant No. EP/M009416/1, Manufacturing Fellowship Grant No. EP/M008975/1, Platform Grant No. EP/N013247/1) and the University of Southampton Zepler Institute Research Collaboration Stimulus Fund [55]. D.C.H. thanks the research collaboration at the University of Glasgow.

## APPENDIX

The backward scattering of the beams due to the periodic refractive-index structure is not included in the calculations because this is ignored safely: (i) Since its period of approximately  $189 \mu\text{m}$  (see Sec. IV B 2) is far greater than the wavelengths used ( $1.49\text{--}1.63 \mu\text{m}$ ), there is no Bragg reflection. (ii) Another type of reflection due to the difference  $\Delta n = n_{\text{as}} - n_{\text{int}}$  between the as-grown-layer refractive index ( $n_{\text{as}}$ ) and the intermixed-layer refractive index ( $n_{\text{int}}$ ) is also ignored because of the very small  $\Delta n$  (i.e.,  $\Delta n/n_{\text{as}} = 0.3\%$ ). This is shown as follows. At an

interface of the domains, we obtain its reflectance  $R_1$  [56]:

$$R_1 = \left( \frac{n_{\text{as}} - n_{\text{int}}}{n_{\text{as}} + n_{\text{int}}} \right)^2 \approx \left( \frac{\Delta n}{2n_{\text{as}}} \right)^2 = 0.0015^2 = 0.0000225 = 0.000225\%. \quad (\text{A1})$$

The transmittance  $T_N$  through  $N$  domains is then calculated as

$$T_N = (1 - R_1)^{N-1}, \quad (\text{A2})$$

where the two ends of the full device are assumed to have perfect antireflection coatings. Since the device length  $L$  is on the order of centimeters for a small pump power (see Fig. 10), if we take  $L \approx 2$  cm, for example, then  $N \approx 2 \text{ cm} / 189 \mu\text{m} \approx 106$ . Inserting Eq. (A1) and  $N \approx 106$  into Eq. (A2), we obtain  $T_N \approx 0.99976378 = 99.976378\%$ , which gives backward reflectance

$$R_N = 1 - T_N \approx 0.00023622 = 0.023622\%. \quad (\text{A3})$$

This is still very small and thus can be ignored safely.

In this paper we deal with the anti-Stokes waves going forward, not backward, by using a phase-matching condition for the forward anti-Stokes-wave generation. Although the backward-beam reflection is not perfectly zero, as seen in Eq. (A3), we can easily distinguish the forward anti-Stokes-wave propagation from the (very little) backward reflection by their propagation directions.

- 
- [1] Y. Fang, N. Seong, and D. D. Dlott, Measurement of the distribution of site enhancements in surface-enhanced Raman scattering, *Science* **321**, 388 (2008).
- [2] S. Nie and S. R. Emory, Probing single molecules and single nanoparticles by surface-enhanced Raman scattering, *Science* **21**, 1102 (1997).
- [3] R. Claps, D. Dimitropoulos, Y. Han, and B. Jalali, Observation of Raman emission in silicon waveguides at  $1.54 \mu\text{m}$ , *Opt. Express* **10**, 1305 (2002).
- [4] R. Claps, D. Dimitropoulos, V. Raghunathan, Y. Han, and B. Jalali, Observation of stimulated Raman amplification in silicon waveguides, *Opt. Express* **11**, 1731 (2003).
- [5] H. Rong, A. Liu, R. Jones, O. Cohen, D. Hak, R. Nicolaescu, A. Fang, and M. Paniccia, An all-silicon Raman laser, *Nature* **433**, 292 (2005).
- [6] H. Rong, R. Jones, A. Liu, O. Cohen, D. Hak, A. Fang, and M. Paniccia, A continuous-wave Raman silicon laser, *Nature* **433**, 725 (2005).
- [7] H. Rong, S. Xu, Y. H. Kuo, V. Sih, O. Cohen, O. Rada, and M. Paniccia, Low-threshold continuous-wave Raman silicon laser, *Nat. Photon.* **1**, 232 (2007).
- [8] M. N. Islam, Raman amplifiers for telecommunications, *IEEE J. Sel. Top. Quantum Electron* **8**, 548 (2002).
- [9] K. Suto, T. Kimura, T. Saito, A. Watanabe, and J. Nishizawa, in *Proceedings of the IEEE Twenty-Fourth International Symposium on Compound Semiconductors, San Diego, USA, 8–11 Sep. 1997* (IEEE, New York, 1998), p. 573.
- [10] D. Cotter, R. J. Manning, K. J. Blow, A. D. Ellis, A. E. Kelly, D. Nasset, I. D. Phillips, A. J. Poustie, and D. C. Rogers, Nonlinear optics for high-speed digital information processing, *Science* **19**, 1523 (1999). Active semiconductor-based switches, p. 1525.
- [11] K. Suto, T. Kimura, T. Saito, and J. Nishizawa, Raman amplification in GaP-Al<sub>x</sub>Ga<sub>1-x</sub>P waveguides for light frequency discrimination, *IEE Proc. Optoelectron.* **145**, 105 (1998).
- [12] N. S. Makarov and V. G. Bespalov, Combined Stokes-anti-Stokes Raman amplification in fiber, *Proc. SPIE* **4605**, 280 (2001).
- [13] J. Reintjes and M. Bashkansky, in *Handbook of Optics: Fiber Optics and Nonlinear Optics* (McGraw Hill, New York, 2001), 2nd ed., Vol. IV, Chap. 18.
- [14] N. S. Makarov and V. G. Bespalov, Effective method of anti-Stokes generation by quasi-phase-matched stimulated Raman scattering, *J. Opt. Soc. Am. B* **22**, 835 (2005).
- [15] P. G. Zverev, T. T. Basiev, V. V. Osiko, A. M. Kulkov, V. N. Voitsekhovskii, and V. E. Yakobson, Physical, chemical and optical properties of barium nitrate Raman crystal, *Opt. Mater.* **11**, 315 (1999).
- [16] Y. H. Kao, M. N. Islam, J. M. Saylor, R. E. Slusher, and W. S. Hobson, Raman effect in AlGaAs waveguides for subpicosecond pulses, *J. Appl. Phys.* **78**, 2198 (1995).
- [17] R. W. Boyd, *Nonlinear Optics* (Academic Press, San Diego, 1992), 1st ed.
- [18] O. Boyraz, D. Dimitropoulos, and B. Jalali, Observation of simultaneous Stokes and anti-Stokes emission in a silicon Raman laser, *IEICE Electron Express* **1**, 435 (2004).
- [19] R. Claps, V. Raghunathan, D. Dimitropoulos, and B. Jalali, Anti-Stokes Raman conversion in silicon waveguides, *Opt. Express* **11**, 2862 (2003).
- [20] K. Iwatsuki and K. Tsukamoto, in *Proceedings of SPIE Conference Vol. 8282, Broadband Access Communication Technologies VI, San Francisco, California, USA, 21 Jan. No. 828202* (SPIE, Bellingham, 2012).
- [21] J. A. Armstrong, N. Bloembergen, J. Ducuing, and P. S. Pershan, Interactions between light waves in a nonlinear dielectric, *Phys. Rev.* **127**, 1918 (1962).
- [22] A. S. Helmy, D. C. Hutchings, T. C. Kleckner, J. H. Marsh, A. C. Bryce, J. M. Arnold, C. R. Stanley, J. S. Aitchison, C. T. A. Brown, K. Moutzouris, and M. Ebrahimzadeh, Quasi phase matching in GaAs-AlAs superlattice waveguides through bandgap tuning by use of quantum-well intermixing, *Opt. Lett.* **25**, 1370 (2000).
- [23] T. C. Kleckner, A. S. Helmy, K. Zeaiter, D. C. Hutchings, and J. S. Aitchison, Dispersion and modulation of the linear optical properties of GaAs-AlAs superlattice waveguides using quantum-well intermixing, *IEEE J. Quantum Electron* **42**, 280 (2006).
- [24] S. J. B. Yoo, C. Caneau, R. Bhat, M. A. Koza, A. Rajhel, and N. Antoniadis, Wavelength conversion by difference frequency generation in AlGaAs waveguides with periodic domain inversion achieved by wafer bonding, *Appl. Phys. Lett.* **68**, 2609 (1996).
- [25] D. C. Hutchings, Modulation of the second-order susceptibility in GaAs/AlAs superlattices, *Appl. Phys. Lett.* **76**, 1362 (2000).

- [26]  $\chi^{(2)}$ -cascaded DFG with  $|2\mathbf{k}_0 - \mathbf{k}_{-1} - \mathbf{k}_1| = 2\pi/\Lambda$ , which can boost the anti-Stokes efficiency, is ignored in our device because this device has small intermediate SHG efficiency for the cascaded DFG.
- [27] M. J. A. Smith, B. T. Kuhlmeier, C. M. de Sterke, C. Wolff, M. Lapine, and C. G. Poulton, Metamaterial control of stimulated Brillouin scattering, *Opt. Lett.* **41**, 2338 (2016).
- [28] G. P. Agrawal, *Nonlinear Fiber Optics* (Academic Press, New York, 2013), 5th ed.
- [29] D. C. Hutchings, Theory of ultrafast nonlinear refraction in semiconductor superlattices, *IEEE J. Sel. Top. Quantum Electron* **10**, 1124 (2004). Secs. IV B and V.
- [30] A. Yariv, *Optical Electronics in Modern Communications* (Oxford University Press, Oxford, 1997), 5th ed. The slowly-varying-envelope approximation with the spatial width  $W$  of propagating pulses greater than their wavelength (1.49–1.63  $\mu\text{m}$ ) can be kept for short pulses with a time width of  $\tau \approx 10$  ps because of  $W = c\tau/\bar{n} = 3 \times 10^8 \text{ m/s} \times 10 \text{ ps}/3.1 \approx 1000 \mu\text{m} \gg 1.49\text{--}1.63 \mu\text{m}$ , where  $c = 3 \times 10^8 \text{ m/s}$  is the velocity of light in a vacuum and  $\bar{n} = 3.1$  is the average refractive index of the device.
- [31] Y. R. Shen and N. Bloembergen, Theory of Stimulated Brillouin and Raman Scattering, *Phys. Rev.* **137**, A1787 (1965).
- [32] P. Weidner and A. Penzkofer, Spectral broadening of picosecond laser pulses in optical fibres, *Opt. Quantum Electron.* **25**, 1 (1993).
- [33] S. J. Wagner, J. Meier, A. S. Helmy, J. S. Aitchison, M. Sorel, and D. C. Hutchings, Polarization-dependent nonlinear refraction and two-photon absorption in GaAs/AlAs superlattice waveguides below the half-bandgap, *J. Opt. Soc. Am. B* **24**, 1557 (2007).
- [34] A. Villeneuve, C. C. Yang, G. I. Stegeman, C. H. Lin, and H. H. Lin, Nonlinear refractive-index and two-photon-absorption near half the band gap in AlGaAs, *Appl. Phys. Lett.* **62**, 2465 (1993).
- [35] M. Dinu, F. Quochi, and H. Garcia, Third-order nonlinearities in silicon at telecom wavelengths, *Appl. Phys. Lett.* **82**, 2954 (2003).
- [36] L. Xu, P. K. A. Wai, and H. Y. Tam, in *Proceedings of the Sixth Chinese Optoelectronics Symposium, Hong Kong University of Science and Technology, Hong Kong, China, 12–14 Sep. 2003* (IEEE, New York, 2003), p. 169.
- [37] W. H. Press, S. A. Teukolsky, W. T. Vetterling, and B. P. Flannery, *Numerical Recipes in C - The Art of Scientific Computing* (Cambridge University Press, Cambridge, 1992), 2nd ed.
- [38] D. C. Hutchings and B. S. Wherrett, Theory of the dispersion of ultrafast nonlinear refraction in zinc-blende semiconductors below the band edge, *Phys. Rev. B* **50**, 4622 (1994).
- [39] D. C. Hutchings and B. S. Wherrett, Theory of the anisotropy of ultrafast nonlinear refraction in zinc-blende semiconductors, *Phys. Rev. B* **52**, 8150 (1995).
- [40] Y. P. Varshni, Temperature dependence of the energy gap in semiconductors, *Physica* **34**, 149 (1967).
- [41] C. Bosio, J. L. Staehli, M. Guzzi, G. Burri, and R. A. Logan, Direct-energy-gap dependence on Al concentration in  $\text{Al}_x\text{Ga}_{1-x}\text{As}$ , *Phys. Rev. B* **38**, 3263 (1988).
- [42] S. Logothetidis, M. Cardona, and M. Garriga, Temperature dependence of the dielectric function and the interband critical-point parameters of  $\text{Al}_x\text{Ga}_{1-x}\text{As}$ , *Phys. Rev. B* **43**, 11950 (1991).
- [43] J. T. Boyd, Theory of parametric oscillation phase matched in GaAs thin-film waveguides, *IEEE J. Quantum Electron.* **8**, 788 (1972).
- [44] M. Illegems and G. L. Pearson, Infrared reflection spectra of  $\text{Ga}_{1-x}\text{Al}_x\text{As}$  mixed crystals, *Phys. Rev. B* **1**, 1576 (1970).
- [45] G. A. Porkolab, P. Apiratikul, B. Wang, S. H. Guo, and C. J. K. Richardson, Low propagation loss AlGaAs waveguides fabricated with plasma-assisted photoresist reflow, *Opt. Express* **22**, 7733 (2014).
- [46] Use of a very small waveguide cross-section area (e.g., 0.1  $\mu\text{m}^2$ ), which is now technically feasible, can greatly reduce the pump power (e.g., to 400 mW). This gives a large structural dispersion to Eq. (69). If this is included to determine the QPM period  $\Lambda$ , the pump power (400 mW) is possible with semiconductor lasers.
- [47] SRS threshold intensity  $\delta$  (e.g., at the maximum observed in Si waveguides [5–7]) is used here because the Raman gain  $g$  is on the same order of magnitude between Si and  $\text{Al}_x\text{Ga}_{1-x}\text{As}$  (or GaAs/AlAs superlattices).
- [48] N. Suzuki, FDTD analysis of two-photon absorption and free-carrier absorption in Si high-index-contrast waveguides, *J. Lightwave Tech.* **25**, 2495 (2007).
- [49] J. S. Aitchison, D. C. Hutchings, J. U. Kang, G. I. Stegeman, and A. Villeneuve, The nonlinear optical properties of AlGaAs at the half band gap, *IEEE J. Quantum Electron.* **33**, 341 (1997).
- [50] I. Tomita, Highly efficient cascaded difference-frequency generation in periodically poled  $\text{LiNbO}_3$  devices with resonators, *IEEE Trans. Electr. Electron. Eng.* **13**, 1214 (2018).
- [51] E. Yablonovitch, Inhibited Spontaneous Emission in Solid-State Physics and Electronics, *Phys. Rev. Lett.* **58**, 2059 (1987).
- [52] S. John, Strong Localization of Photons in Certain Disordered Dielectric Superlattices, *Phys. Rev. Lett.* **58**, 2486 (1987).
- [53] E. Yablonovitch, Photonic crystals: Semiconductors of light, *Sci. Am.* **285**, 46 (2001).
- [54] J. D. Joannopoulos, S. G. Johnson, J. N. Winn, and R. D. Meade, *Photonic Crystals - Molding the Flow of Light* (Princeton University Press, New Jersey, 2008), 2nd ed.
- [55] The data in this paper can be obtained from the University of Southampton ePrint research repository: <http://dx.doi.org/10.5258/SOTON/D0238>.
- [56] J. D. Jackson, *Classical Electrodynamics* (John Wiley & Sons Inc., New York, 1999), 3rd ed.